Molecular basis for gating and regulation of cardiac ryanodine receptor: underlying mechanisms for gain- and loss-of function mutations

Takuya Kobayashi[1,5], Akihisa Tsutsumi[2,5], Nagomi Kurebayashi[1], Kei Saito[3], Masami Kodama[4], Takashi Sakurai[1], Masahide Kikkawa[2], Takashi Murayama[1,*] and Haruo Ogawa[4,6,*]

[1]Department of Cellular and Molecular Pharmacology, Juntendo University Graduate School of Medicine, Tokyo, Japan

[2]Department of Cell Biology and Anatomy, Graduate School of Medicine, The University of Tokyo, Tokyo, Japan

[3]Department of Life Sciences, Graduate School of Arts and Sciences, The University of Tokyo, Tokyo, Japan

[4]Institute for Quantitative Biosciences, The University of Tokyo, Tokyo, Japan

[5]These authors contributed equally

[6]Lead Contact

*Correspondence: Email: takashim@juntendo.ac.jp (T.M.); haru@iqb.u-tokyo.ac.jp (H.O.)

Summary

Cardiac ryanodine receptor (RyR2) is a large Ca^{2+} release channel in the sarcoplasmic reticulum and indispensable for excitation-contraction coupling in the heart. RyR2 is activated by Ca^{2+} and RyR2 mutations have been implicated in severe arrhythmogenic heart diseases. Yet, the structural basis underlying channel opening and how mutations affect the channel remain unknown. Here, we combined high-resolution structures determined by cryo-electron microscopy with quantitative functional analysis of channels carrying various mutations in specific residues. We demonstrated two fundamental mechanisms for channel regulation: interactions close to the channel pore stabilize the channel to prevent hyperactivity and a series of interactions in the surrounding regions is necessary for channel opening upon Ca^{2+} binding. Mutations at the residues involved in the former and the latter mechanisms cause gain-of-function and loss-of-function, respectively. Our results reveal gating mechanisms of the RyR2 channel and alterations by pathogenic mutations at the atomic level.

Keywords

Ryanodine receptor, Membrane protein, calcium channel, cryo-electron microscopy, loss-of-function, gain-of-function, mutation, cardiac muscle, ER/SR membrane, excitation-contraction coupling

Introduction

Cardiac muscle contraction is triggered by an influx of Ca^{2+} into the cytosol through L-type voltage-dependent Ca^{2+} channels in the plasma membrane. This increase in Ca^{2+} activates the cardiac ryanodine receptor (RyR2) in the sarcoplasmic reticulum to release large amount of Ca^{2+}, a process known as Ca^{2+}-induced Ca^{2+} release (CICR) (Endo, 2009; Fabiato and Fabiato, 1978). RyR2 is a homotetramer and the largest ion channel identified to date (Bers, 2004; Santulli et al., 2018). Its total molecular weight is ~2.2 Mda, with each monomer composed of ~5,000 amino acid residues and comprising a large N-terminal mushroom-like structure of the cytoplasmic domain and C-terminal transmembrane (TM) region (Clarke and Hendrickson, 2016; Zalk and Marks, 2017).

In human RyR2, nearly 300 pathogenic mutations have been reported as arrhythmogenic heart diseases, including catecholaminergic polymorphic ventricular tachycardia (CPVT) (Kawamura et al., 2013; Pérez-Riera et al., 2018; Priori et al., 2002; Tester et al., 2004), left ventricular non compaction (LVNF) (Nozaki et al., 2020; Ohno et al., 2014; Tang et al., 2012), and idiopathic ventricular fibrillation (IVF) (Fujii et al., 2017; Jiang et al., 2007; Paech et al., 2014). These mutations alter channel activity to cause either gain-of-function or loss-of-function (Benkusky et al., 2004; Priori and Chen, 2011). However, it remains unclear how these mutations affect the channels at the molecular level.

The first reported structure of RyR2, derived from pig heart, was in the closed state in the presence of EGTA and in the open state with Ca^{2+} and PCB95 (Peng et al., 2016). This was followed by reports on RyR2 activity modulation by regulatory proteins, such as calmodulin (Gong et al., 2019) and FKBP12.6 (Chi et al., 2019). These reports along with prior studies on RyR1 (see (Ogawa et al., 2020) for a recent review) provided insights into RyR2 domain organizations, conformational changes upon channel opening, and the binding sites for ligands and regulatory proteins. Structural analysis has indicated the importance of intra/inter-domain interactions for long-range allosteric regulation of channel gating, yet the roles of individual interaction remains unknown. Thus, the fundamental mechanism underlying channel opening at the atomic level remains to be elucidated. Moreover, it remains unclear how pathogenic mutations alter the channel activity.

To identify key movements and interactions in the channel opening, we here obtained high-resolution structures of recombinant mouse RyR2 by cryo-electron microscopy (EM) single-particle analysis. Then, functional analysis was conducted with RyR2 channels carrying mutations in amino-acid residues in the proposed interactions to clarify their roles during channel gating. Moreover, structures of two mutant channels were determined to address molecular mechanism of alteration. We demonstrated two fundamental mechanisms for channel regulation of RyR2. Interactions for stabilization of the channel in the closed state are located close to the channel pore, while a series of

interactions located in the surrounding regions is necessary for channel opening upon Ca^{2+} binding. Disruption of the former and the latter interactions causes loss-of-function and gain-of-function, respectively. Our results reveal mechanisms underlying channel opening upon Ca^{2+} binding and explain how pathogenic mutations alter channel activity at the atomic level.

RESULTS

Overall conformational changes in RyR2 associated with Ca^{2+} binding

Recombinant mouse RyR2, expressed and purified from HEK293 cells using FKBP12.6 affinity chromatography (Cabra et al., 2016) formed homogeneous tetrameric channels (Figures. S1A and S1B). To precisely trace the Ca^{2+}-induced RyR2 structural changes, a fully open state without any activating ligands other than Ca^{2+} is necessary. Thus, we adopted high salt conditions, which markedly enhance channel activity with Ca^{2+} alone (Figures S1C–S1E) (Meissner, 1994; Ogawa, 1994). We performed cryo-EM single-particle analysis in the presence of 1 mM EGTA and 100 μM Ca^{2+} for closed and open states, respectively. Three-dimensional (3D) classification including focused classification analysis using the TM region revealed two and three classes in the presence of EGTA and Ca^{2+}, respectively (Figures S1F and S1G; Table S1). No major differences were observed among the classes both in the closed and open states. Therefore, subsequent analysis was performed using the class with the highest resolution (before the final classification in the closed state and class 1 in the open state; Table S1). The overall resolution of the final model was 3.3 Å and 3.45 Å for the closed and open states, respectively, and the local resolution for the TM region in the closed state was better than 2.9 Å (Figures S1F and S1G), which allowed us to build precise atomic models and identify specific residues important for channel gating (Figures S1H and S1I). In fact, it was confirmed that the pore was open only by addition of 100 μM of Ca^{2+} (Figure S2A). Conformational changes between closed and open states were large and spanned the entire molecule (Figures 1A, 1B, S2B-S2D; Video S1). Changes associated with Ca^{2+} binding were analyzed in three layers with different heights parallel to the membrane, i.e., the C-terminal domain (CTD), U-motif, and S4-S5 layers (Figures 1C–1E; Video S1). Upon Ca^{2+} binding, CTD rotated clockwise (viewed from cytoplasmic side) (Figure 1C), U-motif rotated clockwise toward the S2-S3 domain (Figure 1D), and S6 leaned outward from the center to open the gate accompanied by rearrangements of S1-S4 helices and outward movement of the S4-S5 linker (Figure 1E). The C-terminal side of the central domain (C-central), U-motif, CTD, and cytoplasmic S6 ($S6_{cyto}$) were tightly attached to each other in both closed and open states (Figures 1F, S2E, and S2F; Video S2) and rotated together 9.8° clockwise with respect to the axis approximately parallel to S6 (Figure 1G). In contrast, the N-terminal side of the

central domain (N-central) did not follow the rotation due to splitting the central domain into two parts with G3987 as the pivot (Figure 1F). Since the rotation axis was close to the Ca^{2+}-binding site, slight movements caused by Ca^{2+} binding resulted in very large movements around S6 (Figure 1G).

Given these series of movements, we hypothesized the gating mechanism of RyR2 as follows: (1) the rotation of the C-central/U-motif/$S6_{cyto}$/CTD complex upon Ca^{2+} binding leads to two downstream pathways for channel pore opening; (2) the $S6_{cyto}$ movement leads to the outward leaning of S6; (3) the U-motif movement leads to sequential movements of the S2-S3 domain and TM segments, causing outward movement of the S4-S5 linker and creating a space where S6 can lean into; and (4) the channel pore finally opens by combining these two independent pathways (Figure 1H). To prove this hypothesis, we performed detailed structural analysis and functional studies.

U-motif/S2-S3 domain interaction is key for signal transduction in response to Ca^{2+} binding

In our hypothesis, the U-motif/S2-S3 domain interaction is important in transducing the rotation of the U-motif in response to TM segment movement (Figure 1D; Videos S1 and S2). We found three key interactions between the U-motif and S2-S3 domain formed by hydrogen bonds or salt bridges (Figures 2A–2C and S3A; Video S3). E4198-K4593-S4167 was evident in the open state, whereas Y4498-K4593 was only formed in the closed state, indicating that K4593 switches the interacting partner between the two states. Additionally, E4193-R4607 was stable in both states.

To clarify the roles of hydrogen bonds/salt bridges in channel gating, functional assays were conducted with recombinant RyR2 carrying mutations at the specific residues (Table 1). Ca^{2+}-dependent [^{3}H]ryanodine binding was used in functional analysis as it reflects channel activity (Fujii et al., 2017; Murayama et al., 2018b). Wild-type (WT) RyR2 exhibited biphasic Ca^{2+}-dependent [^{3}H]ryanodine binding, whereas alanine substitution at K4593 markedly reduced the binding (Figure 2D). Two pathogenic mutations, K4593Q and K4593R, also led to loss of binding (Figures 2E and S3B). Similarly, binding was severely reduced after alanine substitutions (Y4498A, S4167A, and E4198A) and pathogenic mutation (S4167P) in interacting partners (Figures 2D, 2E and S3B). The behaviors of mutant RyR2 channels were also evaluated in live cells by monitoring cytoplasmic and endoplasmic reticulum (ER) luminal Ca^{2+} homeostasis (Fujii et al., 2017; Uehara et al., 2017). In WT RyR2-expressing HEK293 cells, spontaneous Ca^{2+} oscillations occurred with a concomitant decrease in $[Ca^{2+}]_{ER}$, indicating Ca^{2+} release from the ER via RyR2 channels (Figure 2F, left). In contrast, RyR2 channels carrying the K4593A mutation showed no such Ca^{2+} oscillations with increased $[Ca^{2+}]_{ER}$, indicating a loss-of-function of the channel (Figure 2F, right). Similar results were obtained with other

substitutions in S4167, E4198, and K4593 (Figure 2G). Altogether, these results suggest that both E4198-K4593-S4167 and Y4498-K4593 interactions are important for channel opening. We also evaluated the E4193-R4607 interaction and found that alanine substitutions (E4193A and R4607A) and pathogenic mutations (R4607Q and R4607W) led to a loss-of-function of the channel (Figures 2D–2G, S3B). These residues and surrounding sequences are well conserved in all three mammalian RyR subtypes (Figure 2H). These findings indicate that three interactions above S2 in the U-motif/S2-S3 domain interface play a critical role in transducing the Ca^{2+}-binding signal to S2, and that loss of these interactions results in a loss of channel function.

Movements of the S1-S4 bundle lead to outward movement of the S4-S5 linker

Movement of the S2-S3 domain appears to cause S2 movement (see Figure 2C and video S3). This leads to the coordinated 7.6° clockwise rotation of S1, S3, and S4 (Figures 1E, 3A–3C, S4A-S4C; Videos S1 and S4). S1, S2, S3, and S4 are arranged in a circle, placed at equal intervals in a clockwise direction (Figures 3A–3C, S4A-S4C). We found interactions between S1 and S2 (S1/S2), S2/S3, S3/S4, and S1/S4, all of which were maintained in both closed and open states (Figures 3A and 3B, S4A-S4C; Video S4). The hydrophobic interactions between F4497 and L4592 at S1/S2; hydrogen bond between Y4589 and D4715 at S2/S3; hydrogen bond between Y4720 and D4744 at S3/S4; and the salt bridge between R4501 and D4744 at S1/S4 appear to bundle the four TM segments into one (i.e., S1-S4 bundle).

Alanine substitution of residues involved in S1/S2 (F4497 and L4592) and S2/S3 (Y4589 and D4715) interactions exhibited significantly reduced [^{3}H]ryanodine binding (Figures 3D, 3E, and S4G), loss of Ca^{2+} oscillations, and increased ER Ca^{2+} (Figures 3F and 3G)—all indicative of loss-of-function. The pathogenic mutant F4497C also resulted in loss-of-function (Figures 3E, 3G and S4G). Thus, S1/S2 and S2/S3 interactions are necessary for channel opening. In contrast, alanine substitution or pathogenic mutations of residues involved in S1/S4 (R4501 and D4744) and S3/S4 (Y4720 and D4744) interactions caused gain-of-function of the channel with increased [^{3}H]ryanodine binding and reduction in ER Ca^{2+} (Figures 3D-3G, and S4G). Especially, D4744A, which is involved in both interactions, exhibited greatly increased [^{3}H]ryanodine binding with an enhanced Ca^{2+} sensitivity for activation and loss of Ca^{2+} inactivation (Figures 4D, S4I, and S4J). These residues are well conserved in all the mammalian RyR subtypes (Fig. 3O).

Rotation of the S1-S4 bundle causes movement of the S4-S5 linker. We found that the upper part of S4 rotated 40° counterclockwise to form an α-helix upon channel opening, which dramatically changed the position of F4749 (Figures 3H–3J and S4A-S4F; Video S4). The S4-S5 linker, which is

unfolded and significantly bent in the direction of S6 in the closed state, rewinds to an α-helix and moves outward (Figures S4D-S4F; Video S4). A hydrophobic interaction between F4749 in the upper part of S4 and L4505 in S1 was identified in the closed state (Figures 3H and S4A).

Alanine substitutions of residues involved in hydrophobic interactions (L4505A and F4749A) and the pathogenic mutant L4505P caused gain-of-function with increased Ca^{2+} sensitivity and loss of Ca^{2+} inactivation (Figures 3K–3N, S4H-S4J). Notably, no additive effects were observed upon binding of [^{3}H]ryanodine to double mutant L4505A_F4749A (Figure S4H), supporting an interaction between the two residues. Whereas L4505 is conserved in all the mammalian RyR subtypes, F4749 is mutated to valine in the RyR1 subtype (Figure 3O). However, unlike alanine mutant, F4749V exhibited biphasic Ca^{2+} dependent [^{3}H]ryanodine binding with slightly reduced peak value (Figures S4H).

Taking these findings into consideration, we hypothesized a channel opening mechanism in which a series of movements of S4-S5 linker regulate channel opening. In the absence of Ca^{2+}, the channel is stabilized in the closed state as the S4-S5 linker is locked by the "stopper," in form of L4505-F4749 interaction, which prevents α-helix formation of the upper part of S4. The L4505-F4749 interaction is supported by S1/S3 and S3/S4 interactions that keep the two residues appropriately placed. Upon Ca^{2+} binding, clockwise rotation of the S1-S4 bundle induced by U-motif/S2-S3 domain interaction alters the relative positions of L4505 and F4749 to release the stopper. This allows α-helix formation of the upper part of S4 and subsequent outward movement of the S4-S5 linker to open the channel. Loss of necessary interactions, such as that of the U-motif/S2-S3 domain (Figures 2A–2C), S1/S2, and S2/S3 (Figures 3A–3C), cannot release the stopper, leading to loss-of-function (Figures 2D–2G and 3D–3G). Conversely, loss of interactions that support S4, such as S1/S4 and S3/S4 (Figures 3A–3C and 3H–3J) destabilize the channel in the closed state and impart a gain-of-function of the channel (Figures 3D–3G and 3K–3N).

U-motif/S6$_{cyto}$/CTD interaction plays key role in stabilizing the channel in the closed state

The U-motif/S6$_{cyto}$/CTD complex was stable in both the closed and open states (Figure 1F). We found a close contact between U-motif and S6$_{cyto}$ as observed in the closed state structure of RyR1 (Yan et al., 2015) (Figures 4A, 4B, and S5A; Video S5). In the closed state, F4173, V4176, and N4177 in the U-motif and Q4875 and V4879 in S6$_{cyto}$ faced each other forming van der Waals interactions, and were surrounded by Q4876 and Q4878 from S6 (Figure 4B; Video S5). In the open state, S6$_{cyto}$ self-rotated (~30º clockwise at Q4875) and U-motif/S6$_{cyto}$ loosened and appeared unstable (Figure 4C and S5B; Video S5). Buried surface area analysis calculated by CNS (Brünger et al., 1998) demonstrated that the U-motif/S6$_{cyto}$ interface in the open state (362 Å^2) was smaller than in the

closed state (514 $Å^2$). The U-motif also interacted with CTD via F4888, where it penetrated partly into the hydrophobic pocket formed by U-motif F4171, I4172, and V4175 and CTD L4914 (Figure 4D and S5C; Video S5). The U-motif/CTD interaction was stable in both states.

All alanine-substituted mutants of residues interacting between U-motif and $S6_{cyto}$ as well as two CPVT mutations (N4177S and N4177Y) led to gain-of-function (Figures 4E–4H) with mild enhancement in Ca^{2+} sensitivity and severe loss of Ca^{2+} inactivation (Figures S5D, S5F and S5G). Alanine substitution and pathogenic mutation of F4888 exhibited severe gain-of-function with increased Ca^{2+} sensitivity and loss of Ca^{2+} inactivation (Figures 4I–4L, S5E-S5G). Alanine substitution of F4171, I4172, V4175, and L4914—involved in the hydrophobic pocket—also led to milder gain-of-function of the channel than F4888 mutants (Figures 4I–4L, S5E-S5G). Notably, no additive effects were observed with N4177A and F4888A, indicating that U-motif/$S6_{cyto}$ and U-motif/CTD interactions are involved in the common pathways (Figure S5B). All the residues thought to be involved in the U-motif/S6cyto/CTD interactions and surrounding sequences are conserved in mammalian three RyR subtypes (Figure 4M). These findings suggest that interactions within the U-motif/$S6_{cyto}$/CTD complex play a key role in stabilizing the closed state.

Structural basis of the gain-of-function mutations

To elucidate the structural changes associated with mutations, we conducted structural analysis of two gain-of-function mutants (F4888A and F4749A) (Figures S6 and S7). The density for phenyl group of each mutant disappeared clearly (Figures S6B, S6C, S7C, and S7D). Two different classes (closed/open-like structures) were obtained for both mutants in the presence of EGTA (Figures S6 and S7) and Ca^{2+} was bound in the open-like structures. This was not observed for the WT structure in the presence of EGTA, reflecting the result of increasing Ca^{2+} sensitivity in both mutants (Figures 3K and 4I). We also determined the structure in the presence of 100 μM Ca^{2+} for F4749A, and found essentially the same structure as that of open-like F4749A in the presence of EGTA. The overall resolution of the final models was 3.2–3.8 Å (Figures S6A, S7A, and S7B, and Table S1), which was sufficient to analyze structural changes induced by mutations (Figures S6B, S6C, S7C, and S7D).

In the closed structure of F4888A, appreciable change was detected in the U-motif (Figures 5A, 5B, and S6D; Video S6) with no differences in the TM segments and the S4-S5 linker (Figure S6E). Removal of the phenyl group created an extra space above F4171, causing the α-helix in the N-terminal U-motif to rotate ~15° clockwise around F4171 with respect to the WT in the closed state (Figures 5A and 5B; Video S6). Consequently, F4171 moved up to fill the space and the interaction between U-motif and $S6_{cyto}$ became loose, as if the mutant partially mimicked the U-motif

conformational change of the open state WT (Fig. 5A and 5B; Video S6). In the open structure, there was a parallel movement of the U-motif, S2-S3 domain, and S1-S4 toward the outside (Figures 5D and 5E), which differed from the rotational motion observed in the WT structural change from closed to open states. The S4-S5 linker, S5, and S6 showed only a slight outward movement (Figures 5E, S6F, and S6G). Movement of the U-motif in the mutant created a different environment from that of the open state WT U-motif/$S6_{cyto}$ interaction (Figure 5F). Moreover, the buried surface area of the U-motif/$S6_{cyto}$ interface (335 $Å^2$) was smaller than that of the open state WT (362 $Å^2$). These findings are consistent with the idea that the movement of the U-motif is restricted by $S6_{cyto}$ to stabilize the closed state.

In the closed structure of F4749A, removal of the phenyl group had no effect on the structure, and there was no appreciable structural difference from the WT in TM segments and the S4-S5 linker as well as overall structure (Figures 5C and S7E). Although we hypothesized that F4749 and L4505 form a stopper to prevent the rotation of upper part of S4 and subsequent movement of S4-S5 linker (Figure 3), no structural change was detected in the S4-S5 linker in the F4749A mutant. This evidence suggests that the destruction of the stopper itself does not induce spontaneous conformation changes in the S4-S5 linker. In the open state of F4749A, several structural changes were detected (Figure S7F); subtle movements of the S4-S5 linker and S6 (Figures S7G and S7H), a parallel movement of the U-motif, S2-S3 domain (Figure S7I), S1-S4 toward the outside (Figures S7G-S7I), and altered the U-motif/$S6_{cyto}$ interaction (Figure S7J). Thus, similar structural changes were observed for the two mutants with different points of action and this gain-of-function occurred via a common mechanism.

Summary of the Ca^{2+} induced movements in the RyR2

Here, we summarize the channel opening mechanism associated with Ca^{2+} binding of RyR2 determined by high-resolution cryo-EM structures: (1) binding of Ca^{2+} rotates the U-motif/$S6_{cyto}$/CTD complex by 9.8° along with the axis which is 40 Å apart from $S6_{cyto}$; (2) extruding the S2-S3 domain by the U-motif causes S2 to move; (3) movement of S2 rotates the S1-S4 bundle by 7.6° to release the stopper comprising F4749/L4505; (4) rotation of the upper part of S4 allows outward movement of the S4-S5 linker, creating a space where S6 can lean into; and (5) rotation of $S6_{cyto}$ by 30° causes the outward leaning of S6 by 7.8 Å (Figures 5G and 5H). Thus, the sequential rotations of domains/α-helices and domain-domain interactions may occur in conformation changes associated with Ca^{2+} binding.

Discussion

By combining high-resolution cryo-EM structures and quantitative functional analysis of mutant channels, we successfully clarified the gating mechanism of RyR2 upon Ca^{2+} binding. Figure 6A shows a schematic diagram of the channel core domain of RyR2 with details of the important interactions identified in this study. Mutations of residues involved in the signaling pathway for outward movement of the S4-S5 linker caused loss-of-function, whereas those supporting the stopper (i.e., S1/S3/S4 and S1/S4 interactions) or the U-motif/CTD/$S6_{cyto}$ complex led to gain-of-function. Given the locations of these mutations, it becomes apparent that interactions close to the channel pore are important for stabilizing the channel in the closed state and those in the surrounding region are essential for channel opening.

The present results can reasonably explain the gating mechanism of RyR2 channel and how pathogenic or alanine mutations affect the channel activity (Figures 6B-6D). In the closed state of the WT channel, the S4-S5 linker prevents outward leaning of S6 (Figure 6B, left). In addition, $S6_{cyto}$ restricts movement of the U-motif toward the S2-S3 domain. In the open state of the WT, binding of Ca^{2+} moves CTD which transmits signals into two downstream pathways to open the channel; S4-S5 linker is unlocked by sequential conformational changes beginning at the U-motif and S6 leans outward by the movement of $S6_{cyto}$. However, since $S6_{cyto}$ still restricts the U-motif, the activity may be medium (Figure 6B, right). Mutations in the U-motif/S2-S3 domain, S1/S2, or S2/S3 interface disrupt the interaction which is essential for the channel opening (Figure 6C, left). Upon Ca^{2+} binding, conformational changes stop on the way, resulting in loss-of-function (Figure 6C, right). Mutations in S3/S4 or S1/S4 interface unlock the S4-S5 linker (Figure 6D, upper left). However, in the absence of Ca^{2+}, this does not induce spontaneous outward movement of the S4-S5 linker and the channel pore kept closed. In the presence of Ca^{2+}, these channels will show gain-of-function, since the S4-S5 linker is more mobile (Figure 6D, upper right). Mutations in the U-motif/$S6_{cyto}$ or the U-motif/CTD disrupt the U-motif/$S6_{cyto}$ interaction to make the U-motif and $S6_{cyto}$ more mobile (Figure 6D, lower left). Upon Ca^{2+} binding, these channels will show gain-of-function by an increased mobility in the S4-S5 linker and $S6_{cyto}$ (Figure 6D, lower right). Considering that residues involved in the interactions are highly conserved and pathogenic mutations in RyR1 (L4505P, D4744H, and F4888Y; see Table 1) also showed corresponding behaviors, the fundamental mechanism of channel gating may be common among three RyR subtypes.

Outward movement of the S4-S5 linker is important in the channel opening, as it creates the space where S6 can lean into (des Georges et al., 2016; Peng et al., 2016). des Georges et al. (des Georges et al., 2016) provided a more detailed description about the movement of the S4-S5 linker in RyR1; it is bent in the direction of S6 in the closed state, but it straightens and alters its contacts

with S6, thereby opening the channel pore. We showed similar conformational changes in the S4-S5 linker in RyR2 and further demonstrated that rewinding of the upper part of S4 to an α-helix, which is caused by rotation of the S1-S4 bundle, drives the S4-S5 linker movement (Figure 3H-3J and S4D-S4F). Regulatory mechanisms of interaction between the S4-S5 linker and S6 will be the next subject for complete understanding of channel gating.

In RyR1, rearrangement of the salt bridges between S1 (R4563), S3 (Y4791) and S4 (D4815) has been reported to occur upon channel opening (des Georges et al., 2016). We showed that the corresponding salt bridges between R4501, Y4720, and D4744 were preserved in RyR2 but maintained in both closed and open states (Figure 3A-3C and S4A-S4C). Functional assays revealed that hydrogen bonds/salt bridges are critical to keep the stopper in place, as disruption of salt bridges by alanine substitutions or pathogenic mutations caused severe gain-of-function of the channel (Figure 3D-3G and S4G). Interestingly, a recent study showed that diamide insecticides bind to the pocket within the S1-S4 bundle of RyR1, thereby disrupting the salt bridge and opening RyR1 (Ma et al., 2020). Our results reasonably explain why such the insecticides activate the RyR channel.

The U-motif is proposed to be important in channel gating as it forms a stable complex with $S6_{cyto}$ and CTD, which move together when the channel opens (Yan et al., 2015). This movement is accompanied by a rigid shift in the S2-S3 domain, which has been proposed to eventually open the channel pore (Bai et al., 2016). We found that interaction of the U-motif with the S2-S3 domain is critically important in the channel opening; disruption of the interaction causes loss-of-function of the channel (Figure 2 and S3). In addition, we demonstrated that the U-motif/$S6_{cyto}$ interaction stabilizes the channel to the closed state (Figure 4 and S5). Stabilization of the channel is important not only for prevention of the hyperactivity but also for regulation by various stimuli or modifications that activate the channel, e.g., phosphorylation or oxidation/S-nitrosylation (Benkusky et al., 2004; Santulli et al., 2018). The U-motif/$S6_{cyto}$ interaction is the stabilization mechanism first identified at the molecular level and thus may contribute to regulation of the RyR channel.

In RyRs, the large cytoplasmic region is believed to play an important role in regulating channel opening. Indeed, a number of pathogenic mutations is located in the cytoplasmic region. The question arises as to how these mutations, located far from the core domain, cause changes in the channel activity. We demonstrated that the C-Central domain forms a tight complex with the U-motif/$S6_{cyto}$/CTD to move together upon Ca^{2+} binding (Figures 1F, S2E, and S2F). The N-Central domain also moves upon Ca^{2+} binding (Figures 1A and 1F). Through the N-/C-Central domains, the core domain has a series of interactions with the N-terminal domains (NTD), HANDLE, and HD1 domains which consist a major part of the large cytoplasmic region (Peng et al., 2016; Yan et al.,

2015). Thus, it is possible that the conformational changes of the cytoplasmic region by pathogenic mutations affect the channel gating through these interactions. Recently, RyR1 and RyR2 structures carrying gain-of-function mutations at N-terminal domains (NTD) were reported (Iyer et al., 2020). Determining the structures of various mutant RyRs will help to elucidate the long-range allosteric gating mechanism in the future.

In conclusion, we have revealed the gating mechanism of RyR2 upon Ca^{2+} binding and provided structural insights into the effects of pathogenic mutations on channel activity. These findings may greatly help develop more effective drugs to treat RyR2-associated diseases.

Acknowledgements

We thank Mariko Kurakata for assistance with cell culture. We thank Ikue Hiraga and the Laboratory of Radioisotope Research, Research Support Center, Juntendo University Graduate School of Medicine, for technical assistance. We also thank the staff scientists at the University of Tokyo's cryo-EM facility. This study was partly supported by the Japan Society for the Promotion of Sciences KAKENHI (grant number JP16H04748 to H.O., 19K07105 to N.K., and 19H03404 to T.M.); the Platform Project for Supporting Drug Discovery and Life Science Research (Basis for Supporting Innovative Drug Discovery and Life Science Research [BINDS]; grant number JP20am0101080 to H.O. and T.M.); the Practical Research Project for Rare/Intractable Diseases from the Japan Agency for Medical Research and Development (AMED; grant number 19ek0109202) to N.K.); an Intramural Research Grant (29-4 and 2-5) for Neurological and Psychiatric Disorders of NCNP (to T.M.); and the Vehicle Racing Commemorative Foundation (to H.O. and T.M.).

Author contributions

T.K., N.K., T.M., and H.O. conceived and designed the project. M.Ko. and H.O. performed cell culture. T.K. performed protein purification. K.S. performed negative-staining EM studies. A.T. and T.K. prepared the grid for cryo-EM. A.T. and M.Ki. processed the images. H.O. performed model building and refinement. T.M. and N.K. performed the functional analysis. T.K., A.T., N.K., K.S., M.Ko., T.S. M.Ki., T.M., and H.O interpreted the data. T.M. and H.O supervised the project. H.O. and T.M. wrote the manuscript with input from all authors.

Data and Code Availability

Atomic coordinates and cryo-EM density maps have been deposited in the PDB and the Electron Microscopy Data Bank under the accession codes 7FJ6 and EMD-30688 (closed state before

classification), 7FJ7 and EMD-30689 (closed state class1), 7FJ8 and EMD-30690 (closed state class2), 7FJ9 and EMD-30691 (open state class1), 7FJA and EMD-30692 (open state class2), 7FJB and EMD-30693 (open state class3), 7FJD and EMD-30694 (closed-like F4749A mutant in the presence of EGTA), 7FJE and EMD-30695 (open-like F4749A mutant in the presence of EGTA), 7FJF and EMD-30696 (F4749A mutant in the presence of 100 μM of Ca^{2+}), 7FJG and EMD-30697 (closed-like F4888A in the presence of EGTA), and 7FJH and EMD-30698 (open-like F4888A in the presence of EGTA).

Declaration of interests

The authors declare no competing interests.

References

Adams, P.D., Afonine, P.V., Bunkoczi, G., Chen, V.B., Davis, I.W., Echols, N., Headd, J.J., Hung, L.W., Kapral, G.J., Grosse-Kunstleve, R.W.*, et al.* (2010). PHENIX: a comprehensive Python-based system for macromolecular structure solution. Acta Crystallogr D *66*, 213-221.

Afonine, P.V., Poon, B.K., Read, R.J., Sobolev, O.V., Terwilliger, T.C., Urzhumtsev, A., and Adams, P.D. (2018). Real-space refinement in PHENIX for cryo-EM and crystallography. Acta Crystallogr D *74*, 531-544.

Bagattin, A., Veronese, C., Bauce, B., Wuyts, W., Settimo, L., Nava, A., Rampazzo, A., and Danieli, G.A. (2004). Denaturing HPLC-based approach for detecting RYR2 mutations involved in malignant arrhythmias. Clin Chem *50*, 1148-1155.

Bai, X.C., Yan, Z., Wu, J.P., Li, Z.Q., and Yan, N. (2016). The Central domain of RyR1 is the transducer for long-range allosteric gating of channel opening. Cell Res *26*, 995-1006.

Benkusky, N.A., Farrell, E.F., and Valdivia, H.H. (2004). Ryanodine receptor channelopathies. Biochem Biophys Res Commun *322*, 1280-1285.

Bers, D.M. (2004). Macromolecular complexes regulating cardiac ryanodine receptor function. J Mol Cell Cardiol *37*, 417-429.

Bharucha-Goebel, D.X., Santi, M., Medne, L., Zukosky, K., Dastgir, J., Shieh, P.B., Winder, T., Tennekoon, G., Finkel, R.S., Dowling, J.J.*, et al.* (2013). Severe congenital RYR1-associated myopathy: the expanding clinicopathologic and genetic spectrum. Neurology *80*, 1584-1589.

Brünger, A.T., Adams, P.D., Clore, G.M., DeLano, W.L., Gros, P., Grosse-Kunstleve, R.W., Jiang, J.S., Kuszewski, J., Nilges, M., Pannu, N.S.*, et al.* (1998). Crystallography & NMR system: A new software suite for macromolecular structure determination. Acta Crystallogr D *54*, 905-921.

Cabra, V., Murayama, T., and Samsó, M. (2016). Ultrastructural analysis of self-associated RyR2s. Biophys J *110*, 2651-2662.

Chi, X., Gong, D., Ren, K., Zhou, G., Huang, G., Lei, J., Zhou, Q., and Yan, N. (2019). Molecular basis for allosteric regulation of the type 2 ryanodine receptor channel gating by key modulators. Proc Natl Acad Sci U S A *116*, 25575-25582.

Choi, G., Kopplin, L.J., Tester, D.J., Will, M.L., Haglund, C.M., and Ackerman, M.J. (2004). Spectrum and frequency of cardiac channel defects in swimming-triggered arrhythmia syndromes. Circulation *110*, 2119-2124.

Clarke, O.B., and Hendrickson, W.A. (2016). Structures of the colossal RyR1 calcium release channel. Curr Opin Struct Biol *39*, 144-152.

des Georges, A., Clarke, O.B., Zalk, R., Yuan, Q., Condon, K.J., Grassucci, R.A., Hendrickson, W.A., Marks, A.R., and Frank, J. (2016). Structural basis for gating and activation of RyR1. Cell *167*, 145-157.e117.

Eletr, S., and Inesi, G. (1972). Phospholipid orientation in sarcoplasmic membranes: spin-label ESR and proton MNR studies. Biochim Biophys Acta *282*, 174-179.

Emsley, P., Lohkamp, B., Scott, W.G., and Cowtan, K. (2010). Features and development of Coot. Acta Crystallogr D *66*, 486-501.

Endo, M. (2009). Calcium-induced calcium release in skeletal muscle. Physiol Rev *89*, 1153-1176.

Fabiato, A., and Fabiato, F. (1978). Calcium-induced release of calcium from the sarcoplasmic reticulum of skinned cells from adult human, dog, cat, rabbit, rat, and frog hearts and from fetal and new-born rat ventricles. Ann NY Acad Sci *307*, 491-522.

Fujii, Y., Itoh, H., Ohno, S., Murayama, T., Kurebayashi, N., Aoki, H., Blancard, M., Nakagawa, Y., Yamamoto, S., Matsui, Y.*, et al.* (2017). A type 2 ryanodine receptor variant associated with reduced Ca^{2+} release and short-coupled torsades de pointes ventricular arrhythmia. Heart Rhythm *14*, 98-107.

Gong, D.S., Chi, X.M., Wei, J.H., Zhou, G.W., Huang, G.X.Y., Zhang, L., Wang, R.W., Lei, J.L., Chen, S.R.W., and Yan, N. (2019). Modulation of cardiac ryanodine receptor 2 by calmodulin. Nature *572*, 347-351.

Hayashi, M., Denjoy, I., Extramiana, F., Maltret, A., Buisson, N.R., Lupoglazoff, J.M., Klug, D., Hayashi, M., Takatsuki, S., Villain, E.*, et al.* (2009). Incidence and risk factors of arrhythmic events in catecholaminergic polymorphic ventricular tachycardia. Circulation *119*, 2426-2434.

Ibarra M, C.A., Wu, S., Murayama, K., Minami, N., Ichihara, Y., Kikuchi, H., Noguchi, S., Hayashi, Y.K., Ochiai, R., and Nishino, I. (2006). Malignant hyperthermia in Japan: mutation screening of the

entire ryanodine receptor type 1 gene coding region by direct sequencing. Anesthesiology *104*, 1146-1154.

Iyer, K.A., Hu, Y., Nayak, A.R., Kurebayashi, N., Murayama, T., and Samso, M. (2020). Structural mechanism of two gain-of-function cardiac and skeletal RyR mutations at an equivalent site by cryo-EM. Sci Adv *6*, eabb2964.

Jiang, D., Chen, W., Wang, R., Zhang, L., and Chen, S.R. (2007). Loss of luminal Ca^{2+} activation in the cardiac ryanodine receptor is associated with ventricular fibrillation and sudden death. Proc Natl Acad Sci U S A *104*, 18309-18314.

Kawamura, M., Ohno, S., Naiki, N., Nagaoka, I., Dochi, K., Wang, Q., Hasegawa, K., Kimura, H., Miyamoto, A., Mizusawa, Y.*, et al.* (2013). Genetic background of catecholaminergic polymorphic ventricular tachycardia in Japan. Circ J *77*, 1705-1713.

Ma, R., Haji-Ghassemi, O., Ma, D., Jiang, H., Lin, L., Yao, L., Samurkas, A., Li, Y., Wang, Y., Cao, P.*, et al.* (2020). Structural basis for diamide modulation of ryanodine receptor. Nat Chem Biol *16*, 1246-1254.

Mastronarde, D.N. (2005). Automated electron microscope tomography using robust prediction of specimen movements. J Struct Biol *152*, 36-51.

Medeiros-Domingo, A., Bhuiyan, Z.A., Tester, D.J., Hofman, N., Bikker, H., van Tintelen, J.P., Mannens, M.M., Wilde, A.A., and Ackerman, M.J. (2009). The RYR2-encoded ryanodine receptor/calcium release channel in patients diagnosed previously with either catecholaminergic polymorphic ventricular tachycardia or genotype negative, exercise-induced long QT syndrome: a comprehensive open reading frame mutational analysis. J Am Coll Cardiol *54*, 2065-2074.

Meissner, G. (1994). Ryanodine receptor/Ca^{2+} release channels and their regulation by endogenous effectors. Annu Rev Physiol *56*, 485-508.

Murayama, T., Kurebayashi, N., Ishigami-Yuasa, M., Mori, S., Suzuki, Y., Akima, R., Ogawa, H., Suzuki, J., Kanemaru, K., Oyamada, H.*, et al.* (2018a). Efficient high-throughput screening by endoplasmic reticulum Ca^{2+} measurement to identify inhibitors of ryanodine receptor Ca^{2+}-release channels. Mol Pharmacol *94*, 722-730.

Murayama, T., Ogawa, H., Kurebayashi, N., Ohno, S., Horie, M., and Sakurai, T. (2018b). A tryptophan residue in the caffeine-binding site of the ryanodine receptor regulates Ca^{2+} sensitivity. Commun Biol *1*, 98.

Nozaki, Y., Kato, Y., Uike, K., Yamamura, K., Kikuchi, M., Yasuda, M., Ohno, S., Horie, M., Murayama, T., Kurebayashi, N.*, et al.* (2020). Co-phenotype of left ventricular non-compaction cardiomyopathy

and atypical catecholaminergic polymorphic ventricular tachycardia in association with R169Q, a ryanodine receptor type 2 missense mutation. Circ J *84*, 226-234.

Ogawa, H., Kurebayashi, N., Yamazawa, T., and Murayama, T. (2020). Regulatory mechanisms of ryanodine receptor/Ca^{2+} release channel revealed by recent advancements in structural studies. J Muscle Res Cell Motil.

Ogawa, Y. (1994). Role of ryanodine receptors. Crit Rev Biochem Mol Biol *29*, 229-274.

Ohno, S., Omura, M., Kawamura, M., Kimura, H., Itoh, H., Makiyama, T., Ushinohama, H., Makita, N., and Horie, M. (2014). Exon 3 deletion of RYR2 encoding cardiac ryanodine receptor is associated with left ventricular non-compaction. Europace *16*, 1646-1654.

Ozawa, J., Ohno, S., Fujii, Y., Makiyama, T., Suzuki, H., Saitoh, A., and Horie, M. (2018). Differential diagnosis between catecholaminergic polymorphic ventricular tachycardia and long QT syndrome type 1- modified schwartz score. Circ J *82*, 2269-2276.

Paech, C., Gebauer, R.A., Karstedt, J., Marschall, C., Bollmann, A., and Husser, D. (2014). Ryanodine receptor mutations presenting as idiopathic ventricular fibrillation: a report on two novel familial compound mutations, c.6224T>C and c.13781A>G, with the clinical presentation of idiopathic ventricular fibrillation. Pediatr Cardiol *35*, 1437-1441.

Peng, W., Shen, H.Z., Wu, J.P., Guo, W.T., Pan, X.J., Wang, R.W., Chen, S.R.W., and Yan, N. (2016). Structural basis for the gating mechanism of the type 2 ryanodine receptor RyR2. Science *354*.

Pérez-Riera, A.R., Barbosa-Barros, R., de Rezende Barbosa, M.P.C., Daminello-Raimundo, R., de Lucca, A.A., Jr., and de Abreu, L.C. (2018). Catecholaminergic polymorphic ventricular tachycardia, an update. Ann Noninvas Electrocardiol *23*, e12512.

Pettersen, E.F., Goddard, T.D., Huang, C.C., Couch, G.S., Greenblatt, D.M., Meng, E.C., and Ferrin, T.E. (2004). UCSF Chimera--a visualization system for exploratory research and analysis. J Comput Chem *25*, 1605-1612.

Priori, S.G., and Chen, S.R. (2011). Inherited dysfunction of sarcoplasmic reticulum Ca2+ handling and arrhythmogenesis. Circ Res *108*, 871-883.

Priori, S.G., Napolitano, C., Memmi, M., Colombi, B., Drago, F., Gasparini, M., DeSimone, L., Coltorti, F., Bloise, R., Keegan, R.*, et al.* (2002). Clinical and molecular characterization of patients with catecholaminergic polymorphic ventricular tachycardia. Circulation *106*, 69-74.

Rohou, A., and Grigorieff, N. (2015). CTFFIND4: fast and accurate defocus estimation from electron micrographs. J Struct Biol *192*, 216-221.

Roston, T.M., Haji-Ghassemi, O., LaPage, M.J., Batra, A.S., Bar-Cohen, Y., Anderson, C., Lau, Y.R., Maginot, K., Gebauer, R.A., Etheridge, S.P.*, et al.* (2018). Catecholaminergic polymorphic ventricular

tachycardia patients with multiple genetic variants in the PACES CPVT Registry. PLOS ONE *13*, e0205925.

Santulli, G., Lewis, D., des Georges, A., Marks, A.R., and Frank, J. (2018). Ryanodine Receptor Structure and Function in Health and Disease. Subcell Biochem *87*, 329-352.

Shigemizu, D., Aiba, T., Nakagawa, H., Ozaki, K., Miya, F., Satake, W., Toda, T., Miyamoto, Y., Fujimoto, A., Suzuki, Y.*, et al.* (2015). Exome analyses of long QT syndrome reveal candidate pathogenic mutations in calmodulin-interacting genes. PLOS ONE *10*, e0130329.

Smart, O.S., Goodfellow, J.M., and Wallace, B.A. (1993). The pore dimensions of gramicidin A. Biophys J *65*, 2455-2460.

Suzuki, J., Kanemaru, K., Ishii, K., Ohkura, M., Okubo, Y., and Iino, M. (2014). Imaging intraorganellar Ca^{2+} at subcellular resolution using CEPIA. Nat Commun *5*, 4153.

Tang, Y., Tian, X., Wang, R., Fill, M., and Chen, S.R. (2012). Abnormal termination of Ca^{2+} release is a common defect of RyR2 mutations associated with cardiomyopathies. Circ Res *110*, 968-977.

Tester, D.J., Spoon, D.B., Valdivia, H.H., Makielski, J.C., and Ackerman, M.J. (2004). Targeted mutational analysis of the RyR2-encoded cardiac ryanodine receptor in sudden unexplained death: a molecular autopsy of 49 medical examiner/coroner's cases. Mayo Clin Proc *79*, 1380-1384.

Uehara, A., Murayama, T., Yasukochi, M., Fill, M., Horie, M., Okamoto, T., Matsuura, Y., Uehara, K., Fujimoto, T., Sakurai, T.*, et al.* (2017). Extensive Ca^{2+} leak through K4750Q cardiac ryanodine receptors caused by cytosolic and luminal Ca^{2+} hypersensitivity. J Gen Physiol *149*, 199-218.

Wang, D., Shah, K.R., Um, S.Y., Eng, L.S., Zhou, B., Lin, Y., Mitchell, A.A., Nicaj, L., Prinz, M., McDonald, T.V.*, et al.* (2014). Cardiac channelopathy testing in 274 ethnically diverse sudden unexplained deaths. Forensic Sci Int *237*, 90-99.

Wong, L.C., Roses-Noguer, F., Till, J.A., and Behr, E.R. (2014). Cardiac evaluation of pediatric relatives in sudden arrhythmic death syndrome: a 2-center experience. Circ Arrhythm Electrophysiol *7*, 800-806.

Wu, S., Ibarra, M.C., Malicdan, M.C., Murayama, K., Ichihara, Y., Kikuchi, H., Nonaka, I., Noguchi, S., Hayashi, Y.K., and Nishino, I. (2006). Central core disease is due to RYR1 mutations in more than 90% of patients. Brain *129*, 1470-1480.

Yan, Z., Bai, X.C., Yan, C.Y., Wu, J.P., Li, Z.Q., Xie, T., Peng, W., Yin, C.C., Li, X.M., Scheres, S.H.W.*, et al.* (2015). Structure of the rabbit ryanodine receptor RyR1 at near-atomic resolution. Nature *517*, 50-55.

Zalk, R., and Marks, A.R. (2017). Ca^{2+} release channels join the "resolution revolution". Trends Biochem Sci *42*, 543-555.

Zhao, Y., Araki, S., Wu, J., Teramoto, T., Chang, Y.F., Nakano, M., Abdelfattah, A.S., Fujiwara, M., Ishihara, T., Nagai, T.*, et al.* (2011). An expanded palette of genetically encoded Ca^{2+} indicators. Science *333*, 1888-1891.

Zivanov, J., Nakane, T., Forsberg, B.O., Kimanius, D., Hagen, W.J., Lindahl, E., and Scheres, S.H. (2018). New tools for automated high-resolution cryo-EM structure determination in RELION-3. eLife *7*.

Figure legends

Fig. 1. Conformational changes upon Ca^{2+} binding. (A) Overlay of RyR2 in the closed (light blue) and open (yellow) states viewed from the direction parallel to the lipid bilayer and shown as a ribbon model. Two facing protomers in the RyR2 tetramer are shown. (B) Magnified view of the dotted box in (A). In the left protomer, each domain is colored (N-central, light pink; C-central, purple; U-motif, magenta; S1-S5, wheat; S2-S3 domain, light green; S4-S5 linker, warm pink; S6, blue; CTD, orange). S4-S5 linker and S6 moved outside upon Ca^{2+} binding as indicated by the red arrows. Three regions parallel to the membrane are defined as CTD, U-motif, and S4-S5 layers. Ca^{2+}, shown as cyan ball; Zn^{2+}, shown as gray ball. (C–E) Cross-section views of CTD, U-motif, and S4-S5 layers. Closed state is colored in light blue and open state is colored according to (B) or yellow. In (E), Cα representation overlaid with cylindrical TM helices are used. Ca^{2+} binding causes clockwise rotation of CTD (green arrow in C), U-motif (green arrow in D), and S1-S4 TM helices and outward movement of S4-S5 linker and S6 (red arrows in E). (F) C-central/U-motif/$S6_{cyto}$/CTD complex. Closed (light blue) and open (colored according to B) states are overlaid at the CTD. Central domain is split into two parts at G3987 as the pivot upon Ca^{2+} binding. (G) Rotation of the C-central/U-motif/$S6_{cyto}$/CTD complex upon Ca^{2+} binding viewed from the rotation axis. (H) Scheme of channel opening upon Ca^{2+} binding. Two independent pathways via S6 and S4-S5 linker are hypothesized.

Fig. 2. Key interactions between U-motif and S2-S3 domain upon channel opening. (A–C) Interface of U-motif and S2-S3 domain in the closed state (A), open state (B), and an overlay of both states (C) viewed parallel to the membrane and shown as a Cα model. Amino acid residues involved in key interactions are shown as stick models. The color of carbon atoms is the same as that of Cα; oxygen, red; nitrogen, blue. The TM region is indicated in yellow and the region forming α-helices is overlaid with the cylinder model. Hydrogen bonds or salt bridges are shown as orange dotted lines. Density maps around side chains shown in (A) and (B) are superimposed and contoured at 0.025. (D–G) Functional analysis of mutants involved in U-motif/S2-S3 domain interaction. (D) Ca^{2+}-

dependent [^{3}H]ryanodine binding of WT and representative mutants. (E) Summary of [^{3}H]ryanodine binding of WT and mutants at pCa 4.5. (F) Representative traces of cytoplasmic ($[Ca^{2+}]_{cyt}$) and ER ($[Ca^{2+}]_{ER}$) Ca^{2+} signals of HEK293 cells expressing WT or K4593A. Spontaneous Ca^{2+} oscillations occurred with a concomitant decrease in $[Ca^{2+}]_{ER}$ in WT, while the K4593 mutant showed no Ca^{2+} oscillations with an increased $[Ca^{2+}]_{ER}$, indicating loss-of-function of the channel. (G) Summary of upper level of $[Ca^{2+}]_{ER}$ signals in WT and mutants. All mutants showed loss-of-function of the channel. Data are presented as the mean ± SD. *$p < 0.05$; **$p < 0.01$; ***$p < 0.001$. (H) Multiple sequence alignment of three RyR isoforms around the U-motif, S1, and S2 to the initial S2-S3 domain. The gray-shaded residues are the identical sequences among isoforms, and the residues in which mutants were prepared and functional assayed are red-shaded. Secondary structures are shown above the alignment. m, mouse; h, human; p, pig; r, rabbit.

Fig. 3. Key interactions in the transmembrane region upon channel opening. (A–C) The S1-S4 bundle. Closed state (A), open state (B), and overlay of the structures in both states (C) are shown as a Cα model and overlaid with cylinder models. Hydrogen bonds/salt bridges are shown as orange botted lines. Density maps around side chains shown in (A) and (B) are superimposed and contoured at 0.03. (D–G) Functional analysis of mutants involved in the S1/S2, S2/S3, S1/S4, or S3/S4 interaction. (D) Ca^{2+}-dependent [^{3}H]ryanodine binding of WT and representative mutants. (E) Summary of [^{3}H]ryanodine binding of WT and mutants at pCa 4.5. (F) Representative traces of $[Ca^{2+}]_{cyt}$ and $[Ca^{2+}]_{ER}$ signals of HEK293 cells expressing Y4589A or D4744A. (G) Summary of upper level of $[Ca^{2+}]_{ER}$ signals in WT and mutants. (H–J) TM region around S4. Closed state (H), open state (I), and overlay of the structures in both states (J). Structures in both states were fitted to the bottom part of S4 helices and viewed along the axis of the S4 helix and from the cytoplasm; Cα model overlaid with cylinder models. Main chain representation of the S4-S5 linker. Density maps around side chains shown in (H) and (I) are superimposed and contoured at 0.03. (K) Ca^{2+}-dependent [^{3}H]ryanodine binding of WT and representative mutants. (L) Summary of [^{3}H]ryanodine binding of WT and mutants at pCa 4.5. (M) Representative traces of $[Ca^{2+}]_{cyt}$ and $[Ca^{2+}]_{ER}$ signals of HEK293 cells expressing L4505A or F4749A. (N) Summary of upper level of $[Ca^{2+}]_{ER}$ signals in WT and mutants. (O) Multiple sequence alignment of three RyR isoforms around S1, S2, and S3 to S4. The gray-shaded residues are the identical sequences among isoforms, and the residues in which mutants were prepared and functional assayed are red-shaded. Secondary structures are shown above the alignment. m, mouse; h, human; p, pig; r, rabbit.

Fig. 4. Key interactions between the U-motif and $S6_{cyto}$/CTD. (A) Structure around the U-motif in the open state (U-motif, magenta; $S6_{cyto}$, blue; CTD, orange). Ca^{2+} and Zn^{2+} are shown as cyan and gray spheres, respectively. (B, C) Details of the U-motif/$S6_{cyto}$ interaction. Structures in the closed (B) and open (C) states fitted to the N-terminal region of the U-motif are shown as a full atomic model. Density maps around the interaction are superimposed and contoured at 0.025. (D) Details of the U-motif/CTD interaction around F4888. Overly of the structures in the closed (light blue) and open (colored) states. (E–L) Functional analysis of mutants involved in U-motif/$S6_{cyto}$ (E–H) and U-motif/CTD (I–L) interactions. (E, I) Ca^{2+}-dependent [^{3}H]ryanodine binding of WT and representative mutants. (F, J) Summary of [^{3}H]ryanodine binding of WT and mutants at pCa 4.5. (G, K) Representative traces of $[Ca^{2+}]_{cyt}$ and $[Ca^{2+}]_{ER}$ signals of HEK293 cells expressing F4173A or V4879A (G) and F4888A or V4175A (K). (H, L) Summary of upper level of $[Ca^{2+}]_{ER}$ signals in WT and mutants. (M) Multiple sequence alignment of three RyR isoforms around the Umotif and $S6_{cyto}$ to the CTD. The gray-shaded residues are the identical sequences among isoforms, and the residues in which mutants were prepared and functional assayed are red-shaded. Secondary structures are shown above the alignment. m, mouse; h, human; p, pig; r, rabbit.

Fig. 5. Structural basis of gain-of-function mutations and gating mechanism upon Ca^{2+} binding. (A) Structure of closed-like F4888A (colored) overlaid with WT in the closed state (light blue). (B) Enlarged view of the dotted box in (A) superposed with density maps contoured at 0.025. Magenta and green nets represent density maps around WT U-motif in the closed state and closed-like F4888A, respectively. Light blue and blue nets represent density maps around WT $S6_{cyto}$ in the closed state and closed-like F4888A, respectively. (C) Overlay of closed-like F4749A (orange) and WT in the closed state (light blue) at the TM region viewed from the cytoplasm. (D) Interface of U-motif and S2-S3 domain of open-like F4888A (colored) overlaid with WT in the open state (yellow) and in the closed state (only U-motif is shown, blue). Note that in the mutant, parallel movement of the U-motif and S2-S3 domains toward the outside compared with the WT in the open state is completely different from the rotation motion seen in the WT structural change from closed to open state. (E) Overlay of the TM region of open-like F4888A (violet) with WT in the open state (yellow). (F) Details of the U-motif/$S6_{cyto}$ interaction. Open-like F4888A and WT in the open states fitted to the N-terminal region of the U-motif are superposed with density maps contoured at 0.025. Magenta and light pink nets represent density maps around the WT U-motif in the open state and open-like F4888A, respectively. Light blue and orange nets represent density maps around WT $S6_{cyto}$ in the open state and open-like F4888A, respectively. (G, H) Scheme of the structure in the closed (G) and open (H) state. In the

closed state, the upper part of S4 does not form an α-helix. The S4-S5 linker is unfolded and significantly bends in the direction of S6. Binding of Ca^{2+} to the C-central/CTD interface causes 9.8° rotation of the C-central/U-motif/$S6_{cyto}$/CTD complex, leading to two pathways. Pathway 1: the rotation causes 30º rotation of $S6_{cyto}$ which loosens the U-motif/$S6_{cyto}$ interaction and allows outward movement of S6. Pathway 2: a sequential movement of the S2S3 domain, S2, S1-S4 bundle, and S4 allows the upper part of S4 to rewind and form an α-helix. Subsequently, the S4-S5 linker moves outward, creating a space where S6 can lean into. A combination of these two independent pathways eventually leads to opening of the channel.

Fig. 6. Details of interactions and schematic diagram of the RyR2 channel gating mechanism upon Ca^{2+} binding. (A) Details of interactions identified in this study. Amino-acid residues shown in red letter and blue letter indicate gain-of-function and loss-of-function by alanine-substituted or pathogenic mutations, respectively. Arrows indicate interactions. Yellow and dark blue arrows indicate interactions only found in the closed and open states, respectively. (B-D) Schematic diagram of the RyR2 channel gating mechanism upon Ca^{2+} binding. The left and right diagrams show the states in the absence and presence of Ca^{2+}, respectively. The black lines, the domain interactions; The blue T-shaped lines, the domain interactions that act as the suppression; The black lines with arrowhead, the activated domain interactions. The domains shown in gray-scale and colored indicate the domains in the inactive and active states, respectively. (B) Wild type (WT). Since the movement of S4-S5 linker is locked, the channel pore is closed. Ca^{2+} binding unlocks the S4-S5 linker and induces the outward leaning of S6, resulting in the pore opening. (C) Loss-of-function (LOF) mutants. Mutations in the U-motif/S2-S3 domain (#1), S1/S2 (#2) or S2/S3 (#3) interface cause disconnection of signal transduction. Binding of Ca^{2+} therefore cannot induce the outward movement of the S4-S5 linker and the channel pore is kept closed. (D) Gain-of-function (GOF) mutants. (Upper panels) Mutations in S3/S4 (#4) or S1/S4 (#5) interface unlock the S4-S5 linker to be activated. In the absence of Ca^{2+}, the channel pore is kept closed, since the outward leaning of S6 does not occur spontaneously. Binding of Ca^{2+} causes hyperactivity of the channel, since the S4-S5 linker is more active than WT. (Lower panels) Mutations in U-motif, $S6_{cyto}$ or CTD (#6) reduce or lose U-motif/$S6_{cyto}$ interaction. Binding of Ca^{2+} causes hyperactivity of the channel, since S6 and the S4-S5 linker is more active than WT.

Table 1. RyR2 mutants used in this study.

Mutation	Domain	Disease	Ref	Ryanodine binding	ER Ca^{2+} level	Functional change
S4167A	U-motif			↓	↑	LOF
S4167P	U-motif	CPVT (RyR2)	(Ozawa et al., 2018)	↓	↑	LOF
F4171A	U-motif			↑	↓	**GOF**
I4172A	U-motif			↑	↓	**GOF**
F4173A	U-motif			↑	↓	**GOF**
V4175A	U-motif			↑	↓	**GOF**
V4176A	U-motif			↑	↓	**GOF**
N4177A	U-motif			↑	↓	**GOF**
N4177S	U-motif	CPVT (RyR2)	(Medeiros-Domingo et al., 2009)	↑	↓	**GOF**
N4177Y	U-motif	CPVT (RyR2)	(Hayashi et al., 2009)	↑	↓	**GOF**
E4193A	U-motif			↓	↑	LOF
E4198A	U-motif			↓	↑	LOF
F4497A	S1			↓	↑	LOF
F4497C	S1	CPVT (RyR2)	(Choi et al., 2004)	↓	↑	LOF
Y4498A	S1			↓	↑	LOF
R4501A	S1			↑	↓	**GOF**
L4505A	S1			↑	↓	**GOF**
L4505P	S1	CCD (RyR1)	(Wu et al., 2006)	↑	↓	**GOF**
Y4589A	S2			↓	↑	LOF
L4592A	S2			↓	↑	LOF
K4593A	S2-S3			↓	↑	LOF
K4593Q	S2-S3	LQTS (RyR2)	(Shigemizu et al., 2015)	↓	↑	LOF
K4593R	S2-S3	IVF (RyR2)	(Paech et al., 2014)	↓	↑	LOF
R4607A	S2-S3			↓	↑	LOF
R4607Q	S2-S3	Sudden death (RyR2)	(Wong et al., 2014)	↓	↑	LOF
R4607W	S2-S3	Sudden death (RyR2)	(Wang et al., 2014)	↓	↑	LOF
D4715A	S3			↓	↑	LOF
Y4720A	S3			↑	↓	**GOF**
Y4720C	S3	CPVT (RyR2)	(Roston et al., 2018)	↑	↓	**GOF**
D4744A	S4			↑	↓	**GOF**
D4744H	S4	Myopathy (RyR1)	(Bharucha-Goebel et al., 2013)	↑	↓	**GOF**
F4749A	S4			↑	↓	**GOF**
Q4875A	S6cyto			↑	↓	**GOF**
V4879A	S6cyto	CPVT (RyR2)	(Bagattin et al., 2004)	↑	↓	**GOF**
F4888A	CTD			↑	↓	**GOF**
F4888Y	CTD	MH/CCD (RyR1)	(Ibarra M et al., 2006)	↑	↓	**GOF**

L4914A	CTD			↑	↓	**GOF**

CTD, C-terminal domain; CPVT, catecholaminergic polymorphic ventricular tachycardia; CCD, central core disease; LQTS, long QT syndrome; IVF, idiopathic ventricular fibrillation; MH, malignant hyperthermia; LOF, loss-of-function; GOF, gain-of-function.

Materials and methods

Mammalian cell lines and culture conditions

HEK293 cells stably expressing mouse RyR2 (wild type or mutants) were grown in standard DMEM medium (GIBCO), supplemented with 10% fetal bovine serum (FBS) (GIBCO), 100 U/mL penicillin-streptomycin (GIBCO), and maintained in a humidified incubator at 37 ºC with 5% CO2. Growth and protein expression conditions are outlined in Method Details.

Bacterial strains used for protein production

Escherichia coli BL21 cells (Novagen) were used for the expression of the streptavidin-binding peptide (SBP)-tagged FKBP12.6. Growth and protein expression conditions are outlined in Method Details.

Expression and purification of SBP-FKBP12.6

Expression and purification of SBP-tagged FKBP12.6 was performed as described previously (Cabra et al., 2016) with some modifications. Briefly, cDNA for SBP-tagged human FKBP12.6 was subcloned into the pET28 vector (Novagen) containing a 6×His-tag at the N-terminus. *Escherichia coli* BL21 cells transformed with the above expression vector were grown at 37°C in 500 mL LB medium containing ampicillin at a final concentration of 50 mg/L. After reaching an OD_{600} of 0.95–1.2, SBP-FKBP12.6 expression was induced by adding 1 mM IPTG (Wako) for 3 h at 37°C. Cells were then harvested, resuspended in 20 mM MOPS-Na (pH 7.4), 300 mM NaCl, 20 mM imidazole, and a cocktail of protease inhibitors [antipain (Peptide Institute), aprotinin (Nacalai), chymostatin (Peptide Institute), leupeptin (Peptide Institute) and pepstatin A (Peptide Institute), each 2 μg/mL], and lysed using a sonicator in an ice bath. The lysate was centrifuged at 100,000 × *g* for 30 min at 4 °C and the pellet was discarded. The supernatant was incubated for 1 h at 4°C with 0.5 mL Profinity IMAC resin (Bio-Rad Laboratories, Hercules, CA) in a buffer containing 20 mM MOPS-Na (pH 7.4), 300 mM NaCl, and 20 mM imidazole. The resin was washed five times with the buffer and SBP-FKBP12.6 was eluted with buffer containing 300 mM imidazole. The eluted protein was quickly frozen in liquid nitrogen and stored at −80 °C.

Construction of mutant RyR2 cDNA expression vector and generation of stable HEK293 cell lines

Alanine substitution or pathogenic mutations were introduced by inverse PCR using F5 cassette (nucleotide residue number 10,185-14,901 of mouse RyR2) as a template (Uehara et al., 2017). The mutations were confirmed by DNA sequencing. The mutant cassette was inserted into full-length wild-type mouse RyR2 expression vector (pcDNA5/FRT/TO-RyR2wt) (Uehara et al., 2017) by restriction enzymes (*BsiW* I/*Not* I). HEK293 cells stably expressing mutant RyR2 was generated using the Flp-In T-REx system (ThemoFisher) according to manufacturer's instructions. Clones with suitable expression of RyR2 were selected and used for experiments.

Preparation of microsomes from RyR2-expressing HEK293 cells

HEK293 cells stably expressing mouse RyR2 (wild type or mutants) were grown in 60 150-mm cell culture dishes. At 70–80% confluency, protein expression was induced by 2 μg/mL doxycycline (SIGMA) for 48 h. Cells were then harvested, rinsed with cold phosphate-buffered saline (PBS) (GIBCO), and microsomes were prepared as described by Inesi et al. (Eletr and Inesi, 1972). Briefly, the cell pellet was resuspended in 60 mL of 10 mM $NaHCO_3$ in presence of protease inhibitors and processed for nitrogen cavitation for 30 min at 1,000 psi. The suspension was diluted with 60 mL of 0.6 M sucrose, 0.3 M KCl, 40 mM MOPS-Na (pH 7.4), and protease inhibitors and then centrifuged at 1,000 × *g* for 10 min. The supernatant was supplemented with 30 mL of 2.4 M KCl, 0.3 M sucrose, 20 mM MOPS-Na (pH 7.4), and the above protease inhibitor cocktail and centrifuged at 10,000 × *g* for 20 min. The supernatant was then ultracentrifuged at 100,000 × *g* for 30 min. The microsomal pellet was resuspended in 60 mL of 0.6 M KCl, 0.3 M sucrose, 20 mM MOPS-Na (pH 7.4), and the protease inhibitor cocktail, and ultracentrifuged again. Finally, the pellet was resuspended in 12 mL of 0.3 M sucrose, 20 mM MOPS-Na (pH 7.4), and the protease inhibitor cocktail, followed by quick freezing in liquid nitrogen and storage at −80 ℃ until further use.

Purification of RyR2

RyR2 was purified using SBP-FKBP12.6 affinity chromatography (Cabra et al., 2016) with some modifications. The microsomes were solubilized with 2% (w/v) CHAPS (Dojindo) and 1% (w/v) soybean lecithin (Avanti Polar Lipids) in 1 M NaCl, 20 mM MOPS (pH 7.4), 2 mM dithiothreitol, and the protease inhibitor cocktail for 30 min on ice. After centrifugation at 100,000 × *g* for 30 min at 4 °C,

the supernatant was diluted with four volumes of 20 mM MOPS (pH 7.4), 2 mM dithiothreitol, and the protease inhibitor cocktail, after which it was passed through a 0.45-μm filter and loaded onto a pre-equilibrated 5-mL StrepTrap HP column (GE Healthcare, Chicago, IL) with bound SBP-FKBP12.6 fusion protein. The column was successively washed with 10 column volumes of (1) wash buffer (20 mM MOPS pH7.4, 2 mM dithiothreitol, and 0.3 M sucrose) containing 0.2 M NaCl and 0.25% (w/v) CHAPS and (2) wash buffer containing 0.5 M NaCl and 0.015% (w/v) Tween-20 (Sigma-Aldrich). The SBP-FKBP12.6-RyR2 complex was eluted with the wash buffer supplemented with 2.5 mM D-desthiobiotin (Iba Lifesciences). After checking the purity by SDS-PAGE, the eluate was quickly frozen in liquid nitrogen and stored at −80 ℃ until further use.

Negative staining

The purified RyR2 sample was diluted with a buffer containing 0.2 M NaCl, 20 mM MOPS-Na (pH 7.4), 2 mM dithiothreitol, and 0.015% (w/v) Tween-20, and then applied to pre-hydrophilized carbon-coated EM grids (400 mesh hexagonal copper grids, Stork Veco BV, Netherlands), negatively stained with 1.4% (w/v) uranyl acetate solution, and observed at 40,000× magnification using a transmission electron microscope (H7500; Hitachi High-Technologies, Tokyo, Japan) operating at 80 kV. Micrographs were taken at 40,000× using a 1,024 × 1,024 pixel CCD camera (Fast Scan-F114; TVIPS, Gauting, Germany).

Cryo-EM sample preparation

The purified RyR2 sample was buffer-exchanged and concentrated to ~5 mg/mL using Amicon Ultra 100k (Millipore, Burlington, MA) with a buffer containing 0.5 M NaCl, 20 mM MOPS-Na (pH 7.4), 2 mM dithiothreitol, and 0.015% (w/v) Tween-20. EGTA (final concentration of 1 mM) or $CaCl_2$ (final concentration of 100 μM) was added to the concentrated protein samples to fix the channel to the closed or open state. The concentrated RyR2 was loaded onto a Quantifoil Cu/Rh grid (R1.2/1.3, 300 mesh) (Quantifoil), blotted using Vitrobot Mark III (FEI) with 4 s of blotting time and 100% humidity at 6 °C, and then plunge-frozen in liquid ethane.

Cryo-EM data collection

Grids were screened for ice quality and cryo-EM data were acquired using a Titan Krios G3i cryo-EM (Thermo Fisher Scientific, Waltham, MA) running at 300 kV and equipped with a Gatan Quantum-LS

Energy Filter (slit width 25 eV) and a Gatan K3 Summit direct electron detector in the electron counting mode. The electron flux was set to 14 e^-/pix/s at the detector. For the WT close state with EGTA and F4888A with EGTA, imaging was performed at a nominal magnification of 87,000×, corresponding to a calibrated pixel size of 1.07 Å/pix (University of Tokyo, Japan). Electron dose was set to 50 $e^-/Å^2$ for the WT close state and 48 $e^-/Å^2$ for F4888A with EGTA. For other samples, imaging was performed at a nominal magnification of 105,000×, corresponding to a calibrated pixel size of 0.83 Å/pix. Electron dose was set to 60 $e^-/Å^2$. Each movie was subdivided into 1 e^-/frame for all datasets. The data were automatically acquired by the image shift method using SerialEM software (Mastronarde, 2005), with a defocus range of -0.8 to -1.6 μm.

Image processing

Unless otherwise stated, the same procedure was used to process the data. The movie frames were motion corrected by RELION and CTF parameters and estimated by CTFFIND4 (Rohou and Grigorieff, 2015). All the following processes were performed using RELION (ver. 3.0 and 3.1) (Zivanov et al., 2018). To generate 2D templates for automatic particle picking, particles were picked from 100 randomly selected micrographs using template-free Laplacian-of-Gaussian picking, then subjected to multiple rounds of reference-free 2D classification. Good 2D classes were selected as templates and 2D template-based particle picking was performed.

Picked particles were extracted with 4× down-sampling and subjected to one round of 2D classification. Selected good particles from the 2D classification were submitted to 3D classification. After one round of 3D classification, good particles were selected, re-extracted with 1.5× down-sampling, and subjected to 3D refinement. The resulting 3D map and particle set were then subjected to beam-tilt and per-particle defocus refinement, Bayesian polishing, and second round of per-particle defocus refinement followed by 3D refinement. To separate the particles based on open/close states, the no-align 3D classification was performed using a mask covering the TM region. Good classes were subjected to final 3D refinement and postprocessing. Resolution was determined according to the Fourier shell collation (FSC) = 0.143 criterion.

For F4888A EGTA, two datasets were acquired, and particles were combined after Bayesian polishing. In each dataset, particles were selected from one round of 3D classification following two rounds of 2D classification. Detailed information is listed in Supplementary table 1 and described in figs. S2, S13, and S14.

Modelbuilding, refinement, and analysis

Model building was performed using COOT (Emsley et al., 2010). RyR1 in the closed state (PDB accession code, 5TB0) was used as the initial reference model. The coordinates were rigid-body fitted in UCSF Chimera (Pettersen et al., 2004). After substitutions in mouse RyR2 sequence and manual building of the model, real space refinement was performed with PHENIX (Adams et al., 2010; Afonine et al., 2018) with secondary structure and geometry restrained. The residue sequences (1–10, 85–108, 861–864, 954–969, 1,015–1,026, 1,063–1,083, 1,275–1,283, 1,447–1,565, 1,851–1,890, 2,010–2,055, 2,362–2,378, 2,443–2,451, 2,659–2,711, 2,757–2,760, 2,785–2,834, 2,906–2,915, 2,943–2,960, 3,030–3,103, 3,130–3,135, 3,221–3,230, 3,435–3,476, 3,580–3,610, 3,649–3,658, 3,700–3,711, 4,206–4,272, 4,312–4,477, 4,522–4,555, and 4,963–4,966) were omitted, as the corresponding densities were not visible in all of the maps. All figures were prepared using PyMOL (The PyMOL Molecular Graphics System; http://www.pymol.org). Pore radii along the ion conducting pathway were calculated with HOLE (Smart et al., 1993). Buried surface areas were calculated with CNS (Brünger et al., 1998).

[^{3}H]Ryanodine binding

[^{3}H]Ryanodine binding assay was carried out as described previously (Fujii et al., 2017; Murayama et al., 2018a). Briefly, microsomes prepared from HEK293 cells expressing RyR2 were incubated for 1 h at 25 ℃ with 5 nM [^{3}H]ryanodine (PerkinElmer) in reaction media containing 0.17 M NaCl, 20 mM MOPSO-Na (pH 7.0), 2 mM dithiothreitol, 1 mM AMP, and 1 mM $MgCl_2$. Free Ca^{2+} was adjusted with 10 mM EGTA using WEBMAXC STANDARD (https://somapp.ucdmc.ucdavis.edu/pharmacology/bers/maxchelator/webmaxc/webmaxcS.htm).
The [^{3}H]ryanodine binding data (B) were normalized to the maximum number of functional channels (B_{max}), which was separately determined by Scatchard plot analysis using various concentrations (3–20 nM) of [^{3}H]ryanodine in a high-salt medium. The resultant B/B_{max} represents the averaged activity of each mutant.

Single-cell Ca^{2+} imaging

Single-cell Ca^{2+} imaging was performed using HEK293 cells expressing WT or mutant RyR2. In Ca^{2+} measurements with RyR2, the Ca^{2+} signals from the cytoplasm ($[Ca^{2+}]_{cyt}$) and ER lumen ($[Ca^{2+}]_{ER}$) were monitored using G-GECO1.1 (a gift from Robert Campbell from University of Alberta; Addgene

plasmid #32445) (Zhao et al., 2011). and R-CEPIA1er (a gift from Masamitsu Iino, Nihon University, Tokyo, Japan; Addgene plasmid #58216) (Suzuki et al., 2014), respectively. Cells were transfected with cDNAs for these Ca^{2+} indicators 26–30 h before measurement and at the same time doxycycline (2 μg/mL) was added to the culture medium to induce RyR2 expression. Experiments were carried out in HEPES-buffered Krebs solution (140 mM NaCl, 5 mM KCl, 2 mM $CaCl_2$, 1 mM $MgCl_2$, 11 mM glucose, and 5 mM HEPES at pH 7.4). At the end of each experiment, F_{min} and F_{max} were obtained with 0Ca Krebs solution containing 20 μM ionomycin, 5 mM BAPTA, and 20 μM cyclopiazonic acid and 20Ca Krebs solution containing 20 μM ionomycin and 20 mM $CaCl_2$, respectively (Uehara et al., 2017). The fluorescence signal ($F-F_{min}$) was normalized to the maximal fluorescence intensity ($F_{max}-F_{min}$). Measurements were carried out at 26 °C.

Titles for multimedia files

Video S1.

The architecture of RyR2 and details of its opening.

Video S2.

Rotation of C-central/U-motif/U-motif/$S6_{cyto}$/CTD complex upon Ca^{2+} binding.

Video S3.

Details of signal transmission from the cytoplasm into the TM region via the U-motif/S2-S3 domain interaction.

Video S4.

Conformation changes in the TM region upon Ca^{2+} binding.

Video S5.

Details of the U-motif/$S6_{cyto}$/CTD interaction.

Video S6.

Structure comparison of the F4888A mutant with the WT in the closed state.

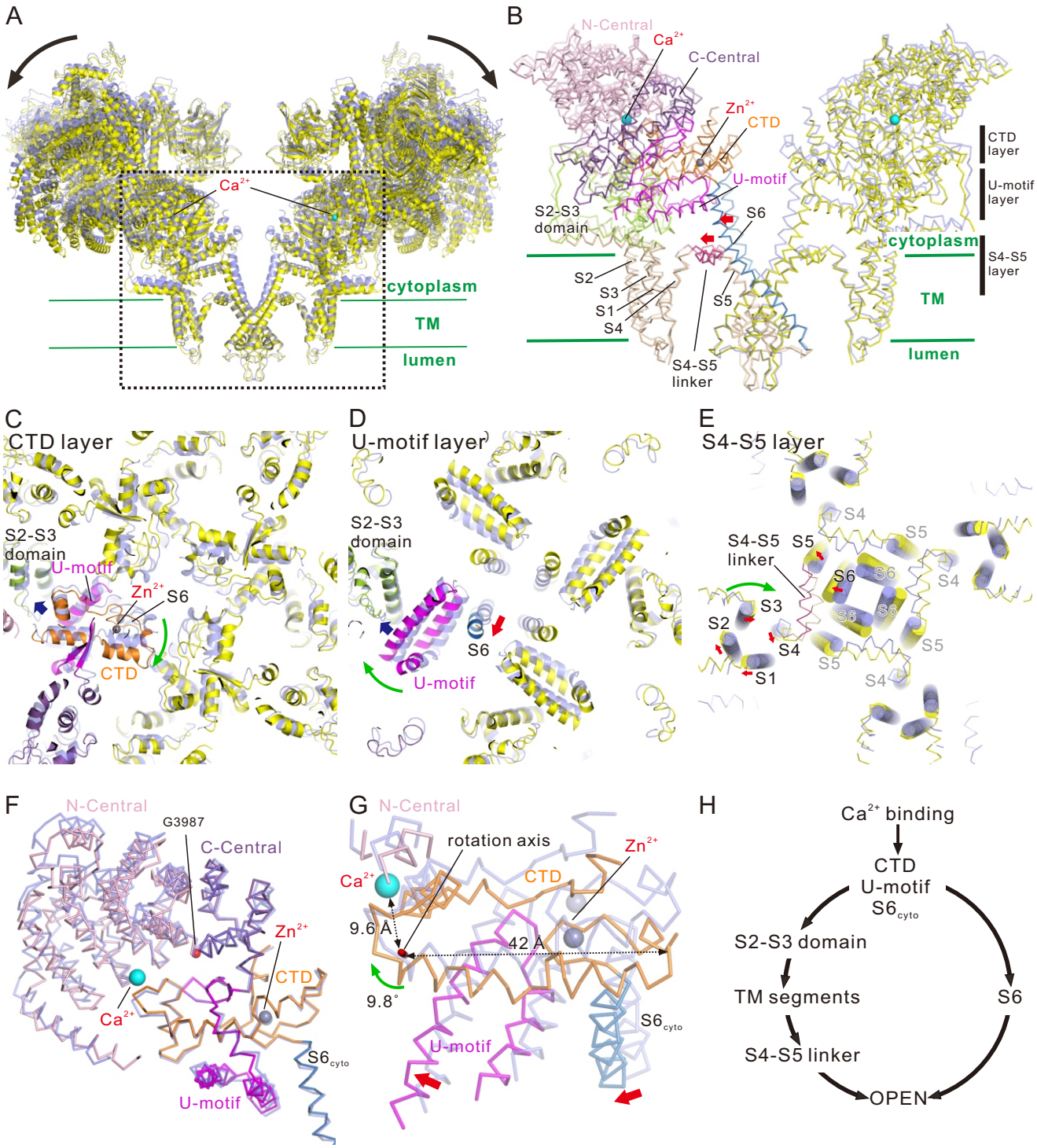
A
Ca2+
cytoplasm
TM
lumen
B
N-Central
Ca2+
C-Central
Zn2+
CTD
U-motif
S6
S2-S3
domain
S2
S3
S1
S4
S5
S4-S5
linker
CTD
layer
U-motif
layer
cytoplasm
S4-S5
layer
TM
lumen
C
CTD layer
S2-S3
domain
U-motif
Zn2+
S6
CTD
D
U-motif layer
S2-S3
domain
S6
U-motif
E
S4-S5 layer
S4-S5
linker
S5
S6
S4
S3
S2
S1
F
N-Central
G3987
C-Central
Zn2+
CTD
Ca2+
S6cyto
U-motif
G
N-Central
rotation axis
Zn2+
Ca2+
CTD
9.6 Å
42 Å
9.8°
S6cyto
U-motif
H
Ca2+ binding
CTD
U-motif
S6cyto
S2-S3 domain
TM segments
S4-S5 linker
S6
OPEN

Figure 1

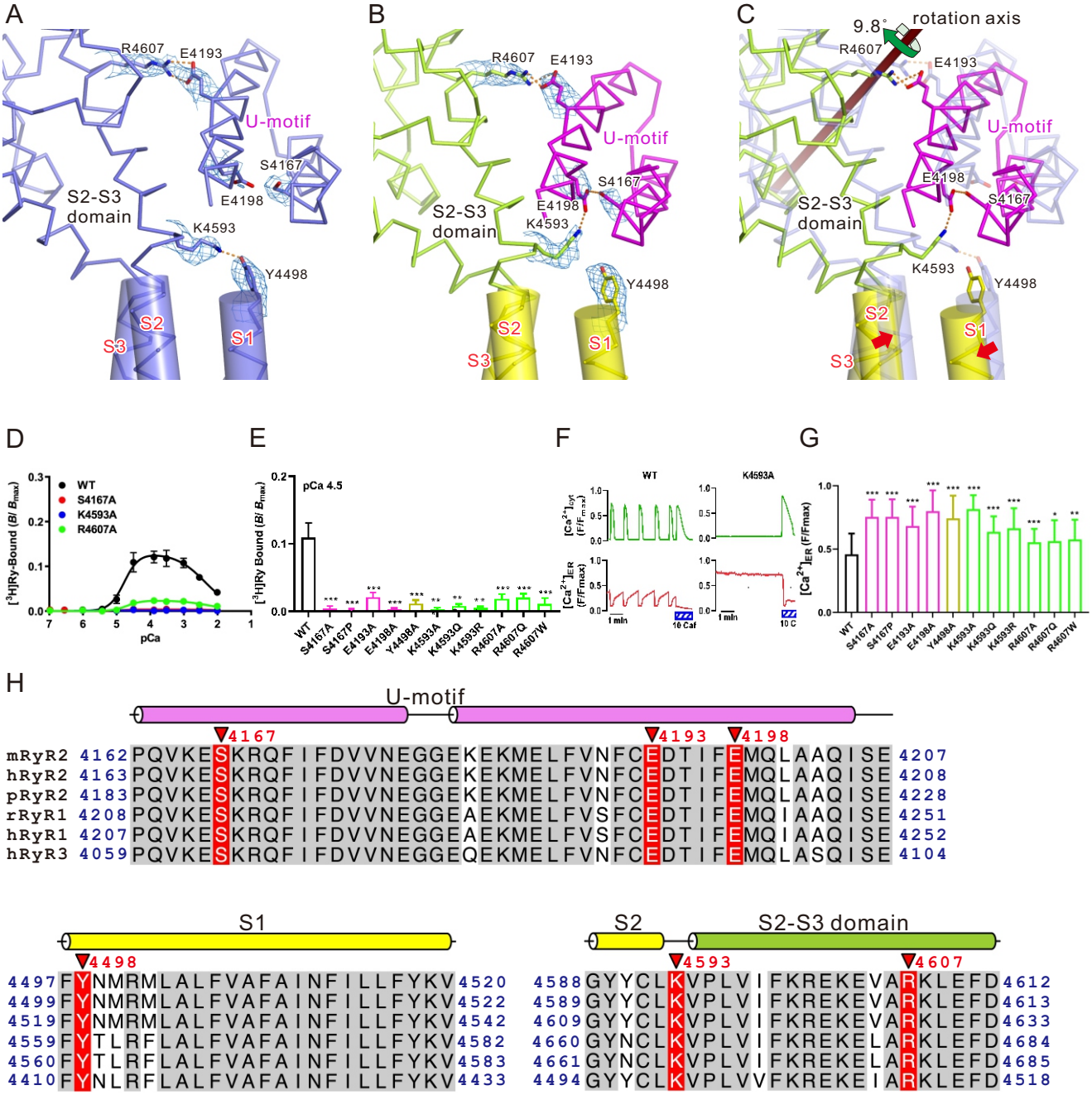
A
R4607
E4193
U-motif
S4167
E4198
S2-S3
domain
K4593
Y4498
S2
S3
S1
B
R4607
E4193
U-motif
S4167
E4198
S2-S3
domain
K4593
Y4498
S2
S3
S1
C
9.8°
rotation axis
R4607
E4193
U-motif
E4198
S4167
S2-S3
domain
K4593
Y4498
S2
S3
S1
D
WT
S4167A
K4593A
R4607A
[3H]Ry-Bound (B/ Bmax)
pCa
E
pCa 4.5
[3H]Ry Bound (B/ Bmax)
WT
S4167A
S4167P
E4193A
E4198A
Y4498A
K4593A
K4593Q
K4593R
R4607A
R4607Q
R4607W
F
WT
K4593A
1 min
10 Caf
10 C
G
[Ca2+]ER (F/Fmax)
H
U-motif
4167
4193
4198
mRyR2 4162 PQVKESKRQFIFDVVNEGGEKEKMELFVNFCEDTIFEMQLAAQISE 4207
hRyR2 4163 PQVKESKRQFIFDVVNEGGEKEKMELFVNFCEDTIFEMQLAAQISE 4208
pRyR2 4183 PQVKESKRQFIFDVVNEGGEKEKMELFVNFCEDTIFEMQLAAQISE 4228
rRyR1 4208 PQVKESKRQFIFDVVNEGGEAEKMELFVSFCEDTIFEMQIAAQISE 4251
hRyR1 4207 PQVKESKRQFIFDVVNEGGEAEKMELFVSFCEDTIFEMQIAAQISE 4252
hRyR3 4059 PQVKESKRQFIFDVVNEGGEQEKMELFVNFCEDTIFEMQLASQISE 4104
S1
4498
4497 FYNMRMLALFVAFAINFILLFYKV 4520
4499 FYNMRMLALFVAFAINFILLFYKV 4522
4519 FYNMRMLALFVAFAINFILLFYKV 4542
4559 FYTLRFLALFVAFAINFILLFYKV 4582
4560 FYTLRFLALFVAFAINFILLFYKV 4583
4410 FYNLRFLALFVAFAINFILLFYKV 4433
S2
S2-S3 domain
4593
4607
4588 GYYCLKVPLVIFKREKEVARKLEFD 4612
4589 GYYCLKVPLVIFKREKEVARKLEFD 4613
4609 GYYCLKVPLVIFKREKEVARKLEFD 4633
4660 GYNCLKVPLVIFKREKELARKLEFD 4684
4661 GYNCLKVPLVIFKREKELARKLEFD 4685
4494 GYYCLKVPLVVFKREKEIARKLEFD 4518

Figure 2

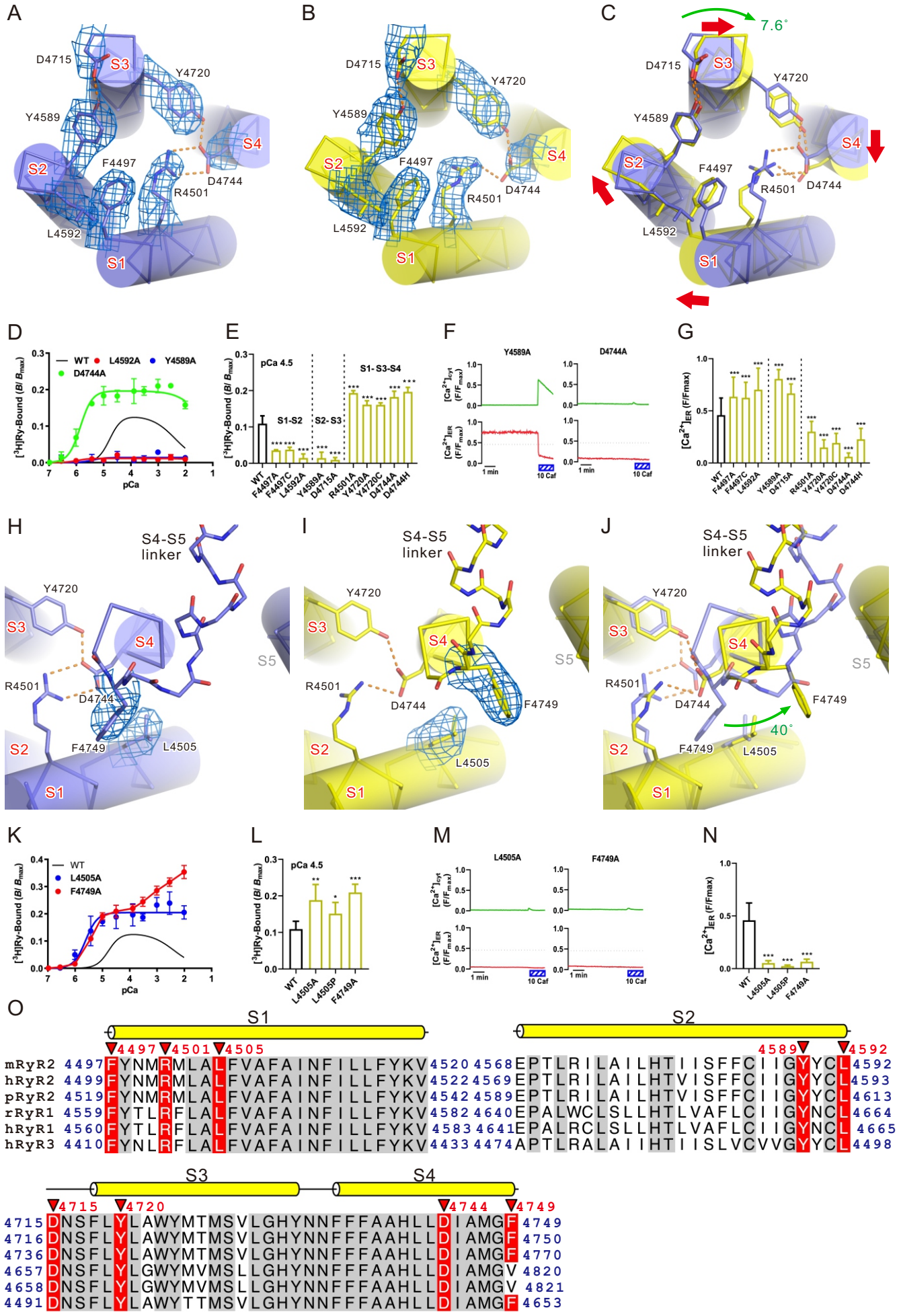
A
D4715
S3
Y4720
Y4589
S4
S2
F4497
D4744
R4501
L4592
S1
B
D4715
S3
Y4720
Y4589
S2
F4497
S4
D4744
R4501
L4592
S1
C
7.6˚
D4715
S3
Y4720
Y4589
S4
S2
F4497
R4501
D4744
L4592
S1
D
WT
L4592A
Y4589A
D4744A
[3H]Ry-Bound (B/ Bmax)
pCa
E
pCa 4.5
S1-S2
S2-S3
S1-S3-S4
[3H]Ry-Bound (B/ Bmax)
WT
F4497A
F4497C
L4592A
Y4589A
D4715A
R4501A
Y4720A
Y4720C
D4744A
D4744H
F
Y4589A
D4744A
[Ca2+]cyt (F/Fmax)
[Ca2+]IER (F/Fmax)
1 min
10 Caf
G
[Ca2+]IER (F/Fmax)
H
S4-S5 linker
Y4720
S3
S4
S5
R4501
D4744
S2
F4749
L4505
S1
I
S4-S5 linker
Y4720
S3
S4
S5
R4501
D4744
F4749
S2
L4505
S1
J
S4-S5 linker
Y4720
S3
S4
S5
R4501
D4744
F4749
40˚
S2
F4749
L4505
S1
K
WT
L4505A
F4749A
[3H]Ry-Bound (B/ Bmax)
pCa
L
pCa 4.5
[3H]Ry-Bound (B/ Bmax)
WT
L4505A
L4505P
F4749A
M
L4505A
F4749A
[Ca2+]cyt (F/Fmax)
[Ca2+]IER (F/Fmax)
1 min
10 Caf
N
[Ca2+]IER (F/Fmax)
WT
L4505A
L4505P
F4749A
O
S1
S2
4497 4501 4505
4589 4592
mRyR2 4497 FYNMRMLALFVAFAINFILLFYKV 4520 4568 EPTLRILAILHTIISFFCIIGYYCL 4592
hRyR2 4499 FYNMRMLALFVAFAINFILLFYKV 4522 4569 EPTLRILAILHTVISFFCIIGYYCL 4593
pRyR2 4519 FYNMRMLALFVAFAINFILLFYKV 4542 4589 EPTLRILAILHTVISFFCIIGYYCL 4613
rRyR1 4559 FYTLRFLALFVAFAINFILLFYKV 4582 4640 EPALWCLSLLHTLVAFLCIIGYNCL 4664
hRyR1 4560 FYTLRFLALFVAFAINFILLFYKV 4583 4641 EPALRCLSLLHTLVAFLCIIGYNCL 4665
hRyR3 4410 FYNLRFLALFVAFAINFILLFYKV 4433 4474 APTLRALAIIHTIISLVCVVGYYCL 4498
S3
S4
4715 4720 4744 4749
4715 DNSFLYLAWYMTMSVLGHYNNFFFAAHLLDIAMGF 4749
4716 DNSFLYLAWYMTMSVLGHYNNFFFAAHLLDIAMGF 4750
4736 DNSFLYLAWYMTMSVLGHYNNFFFAAHLLDIAMGF 4770
4657 DNSFLYLGWYMVMSLLGHYNNFFFAAHLLDIAMGV 4820
4658 DNSFLYLGWYMVMSLLGHYNNFFFAAHLLDIAMGV 4821
4491 DNSFLYLAWYTTMSVLGHYNNFFFAAHLLDIAMGF 4653

Figure 3

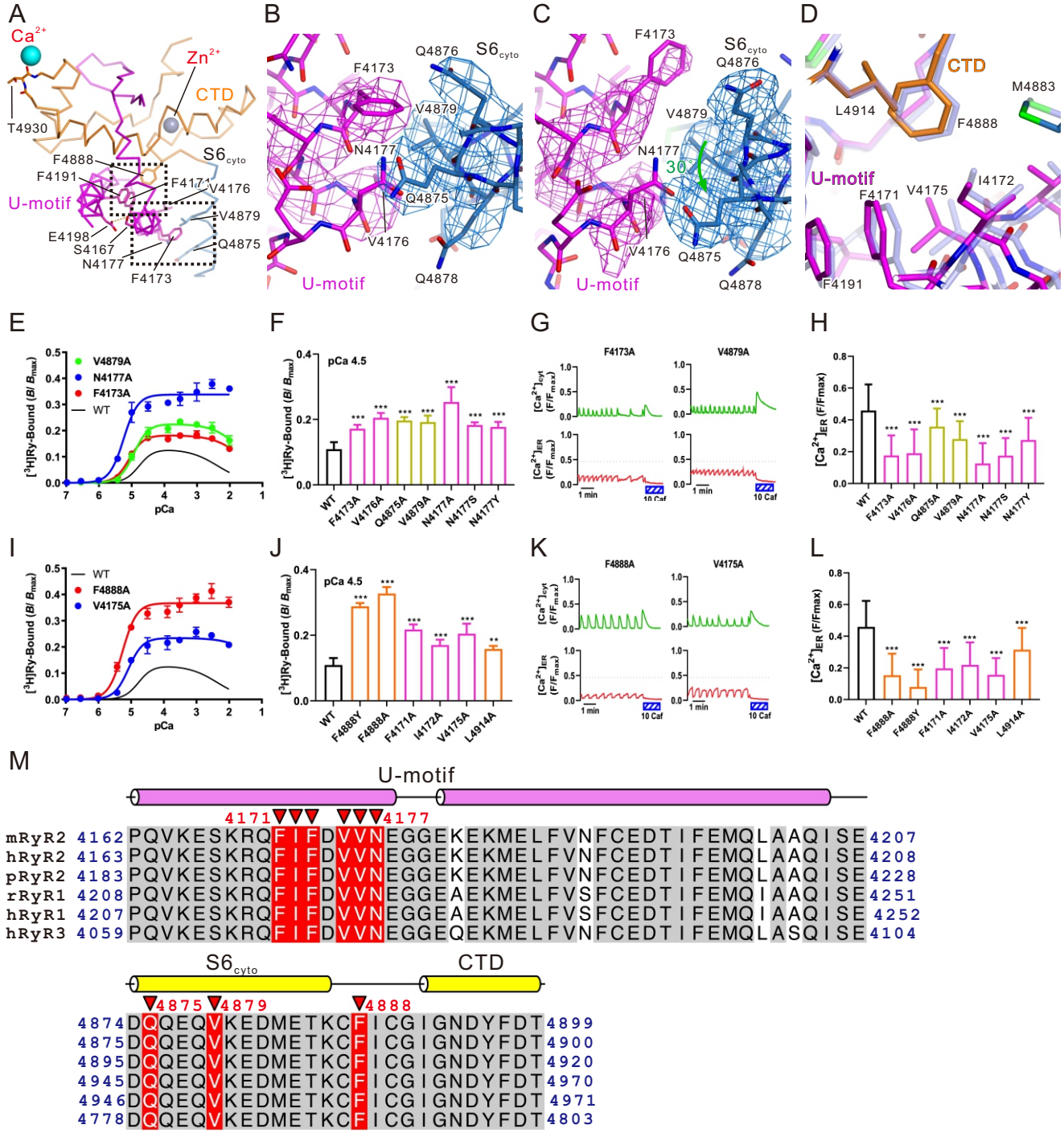
A
Ca2+
Zn2+
CTD
T4930
S6cyto
F4888
F4191
F4171
V4176
U-motif
V4879
E4198
S4167
N4177
Q4875
F4173
B
Q4876
S6cyto
F4173
V4879
N4177
Q4875
V4176
U-motif
Q4878
C
F4173
S6cyto
Q4876
V4879
N4177
30°
V4176
Q4875
U-motif
Q4878
D
CTD
M4883
L4914
F4888
U-motif
F4171
V4175
I4172
F4191
E
V4879A
N4177A
F4173A
WT
[3H]Ry-Bound (B/ Bmax)
pCa
F
pCa 4.5
WT
F4173A
V4176A
Q4875A
V4879A
N4177A
N4177S
N4177Y
G
F4173A
V4879A
1 min
10 Caf
H
[Ca2+]ER (F/Fmax)
I
WT
F4888A
V4175A
J
pCa 4.5
WT
F4888Y
F4888A
F4171A
I4172A
V4175A
L4914A
K
F4888A
V4175A
L
M
U-motif
4171
4177
mRyR2 4162 PQVKESKRQFIFDVVNEGGEKEKMELFVNFCEDTIFEMQLAAQISE 4207
hRyR2 4163 PQVKESKRQFIFDVVNEGGEKEKMELFVNFCEDTIFEMQLAAQISE 4208
pRyR2 4183 PQVKESKRQFIFDVVNEGGEKEKMELFVNFCEDTIFEMQLAAQISE 4228
rRyR1 4208 PQVKESKRQFIFDVVNEGGEAEKMELFVSFCEDTIFEMQIAAQISE 4251
hRyR1 4207 PQVKESKRQFIFDVVNEGGEAEKMELFVSFCEDTIFEMQIAAQISE 4252
hRyR3 4059 PQVKESKRQFIFDVVNEGGEQEKMELFVNFCEDTIFEMQLASQISE 4104
S6cyto
CTD
4875
4879
4888
4874 DQQEQVKEDMETKCFICGIGNDYFDT 4899
4875 DQQEQVKEDMETKCFICGIGNDYFDT 4900
4895 DQQEQVKEDMETKCFICGIGNDYFDT 4920
4945 DQQEQVKEDMETKCFICGIGNDYFDT 4970
4946 DQQEQVKEDMETKCFICGIGNDYFDT 4971
4778 DQQEQVKEDMETKCFICGIGNDYFDT 4803

Figure 4

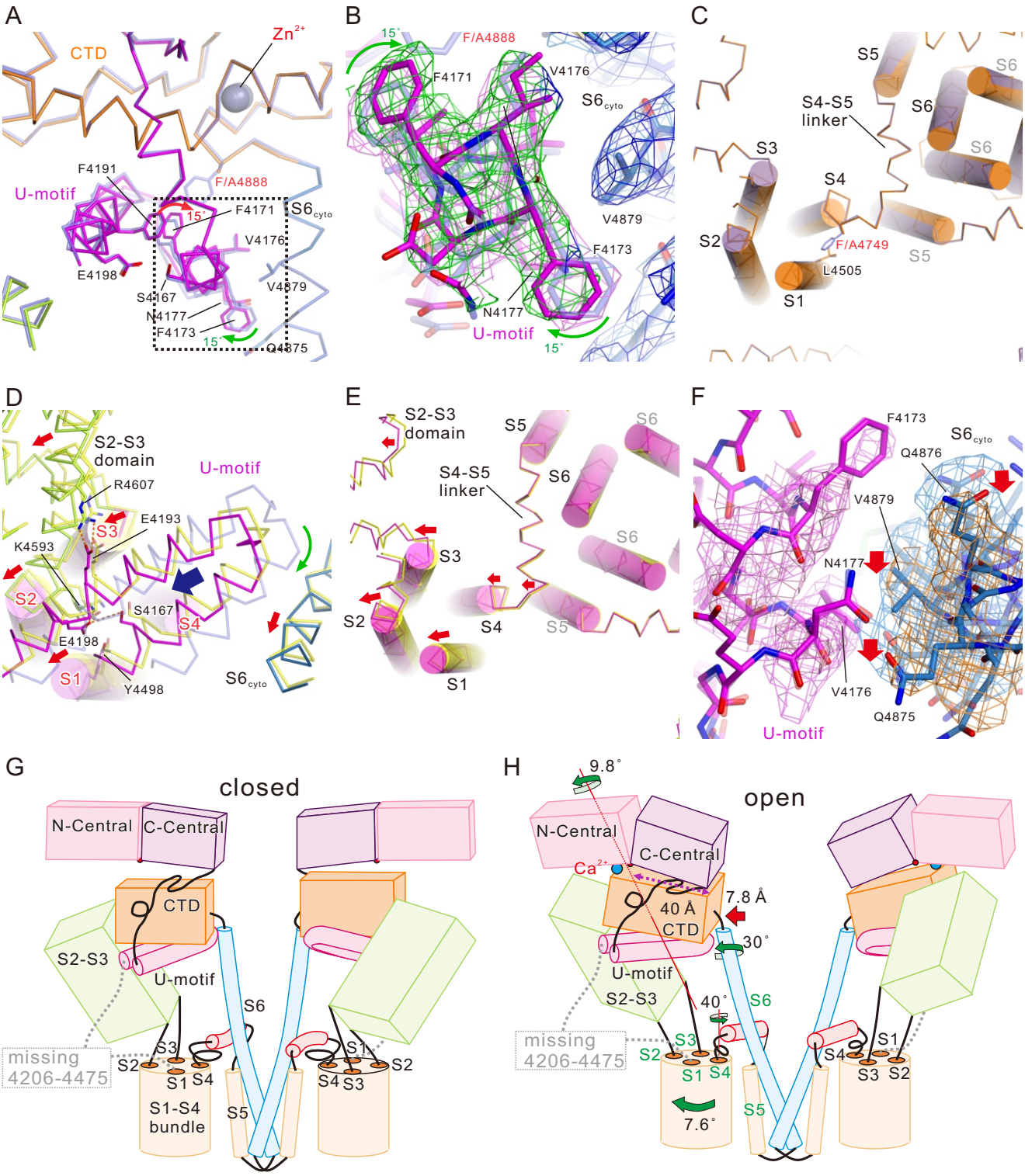
A
CTD
Zn2+
F4191
U-motif
F/A4888
15˚
F4171
S6cyto
V4176
E4198
S4167
V4879
N4177
F4173
15˚
Q4875
B
15˚
F/A4888
F4171
V4176
S6cyto
V4879
F4173
N4177
U-motif
15˚
C
S5
S6
S4-S5
linker
S6
S3
S6
S4
S2
F/A4749
S5
L4505
S1
D
S2-S3
domain
U-motif
R4607
E4193
S3
K4593
S2
S4167
S4
E4198
S1
Y4498
S6cyto
E
S2-S3
domain
S5
S6
S4-S5
linker
S6
S6
S3
S2
S4
S5
S1
F
F4173
S6cyto
Q4876
V4879
N4177
V4176
Q4875
U-motif
G
closed
N-Central
C-Central
CTD
S2-S3
U-motif
S6
missing
4206-4475
S3
S2
S1
S4
S1-S4
bundle
S5
S1
S2
S4
S3
H
9.8˚
open
N-Central
C-Central
Ca2+
7.8 Å
40 Å
CTD
30˚
U-motif
S2-S3
40˚
S6
missing
4206-4475
S3
S2
S1
S4
7.6˚
S5
S1
S4
S3
S2

Figure 5

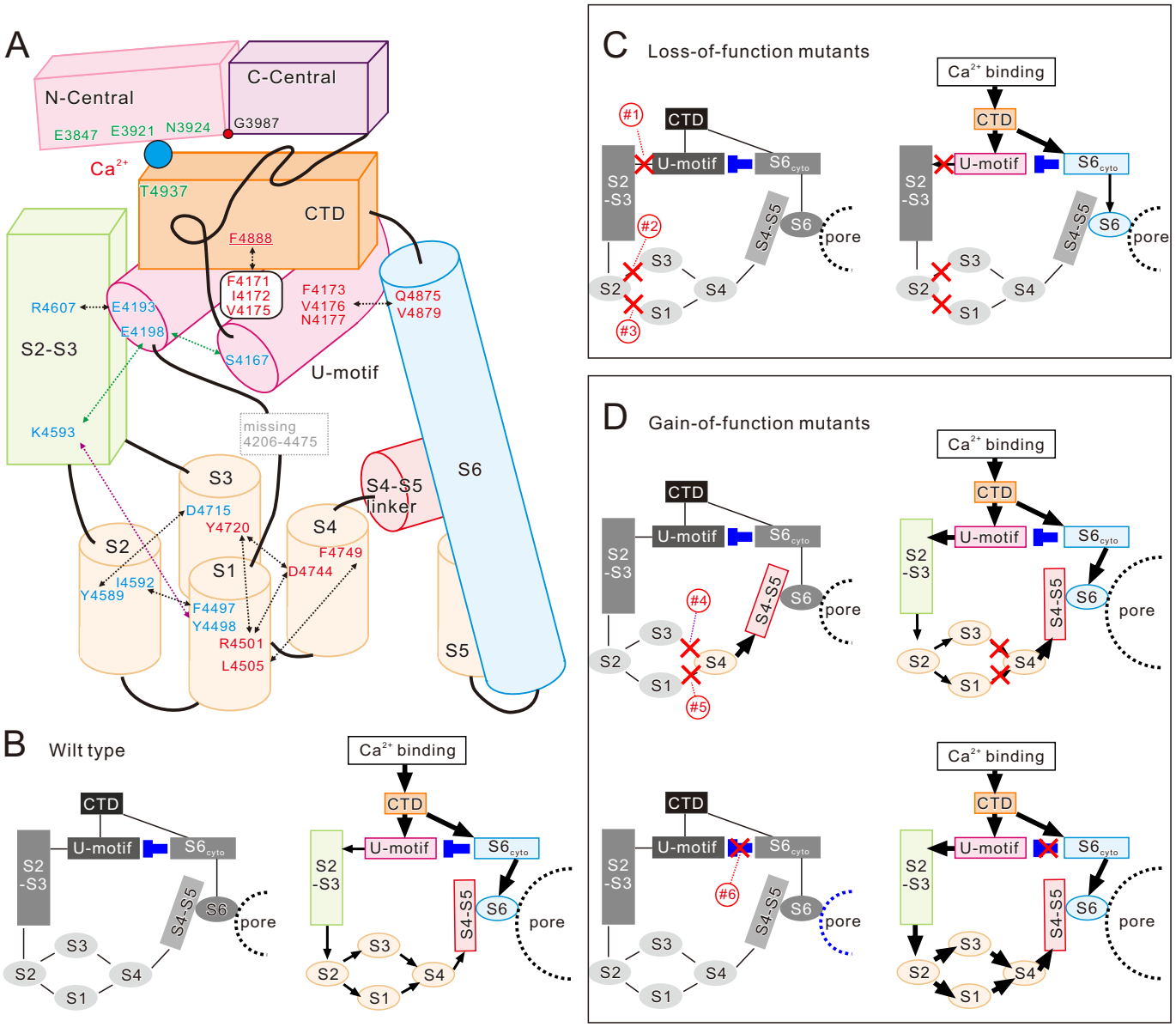
A
N-Central
C-Central
E3847
E3921
N3924
G3987
Ca2+
T4937
CTD
F4888
F4171
I4172
V4175
F4173
V4176
N4177
Q4875
V4879
R4607
E4193
E4198
S4167
S2-S3
U-motif
K4593
missing
4206-4475
S3
S4-S5
linker
S6
D4715
Y4720
S4
F4749
S2
I4592
Y4589
S1
D4744
F4497
Y4498
R4501
L4505
S5
B
Wilt type
CTD
U-motif
S6cyto
S2
-S3
S4-S5
S6
pore
S3
S2
S4
S1
Ca2+ binding
C
Loss-of-function mutants
#1
#2
#3
D
Gain-of-function mutants
#4
#5
#6

Figure 6